

# Sunspot Rotation Leading to Coronal Mass Ejection

**Chaowei Jiang** (✉ [chaowei@hit.edu.cn](mailto:chaowei@hit.edu.cn))

Harbin Institute of Technology, Shenzhen <https://orcid.org/0000-0002-7018-6862>

**xueshang feng**

Chinese academy of sciences <https://orcid.org/0000-0001-8605-2159>

**Xinkai Bian**

Harbin Institute of Technology, Shenzhen

**Peng Zou**

Harbin Institute of Technology, Shenzhen

**Aiying Duan**

Sun Yat-sen University

**Xiaoli Yan**

Yunnan Observatories, CAS <https://orcid.org/0000-0003-2891-6267>

**Qiang Hu**

The University of Alabama in Huntsville

**Wen He**

The University of Alabama in Huntsville

**Pingbing Zuo**

Harbin Institute of Technology, Shenzhen

**Yi Wang**

Harbin Institute of Technology, Shenzhen

---

## Article

### Keywords:

**Posted Date:** May 12th, 2022

**DOI:** <https://doi.org/10.21203/rs.3.rs-1613867/v1>

**License:**   This work is licensed under a Creative Commons Attribution 4.0 International License.

[Read Full License](#)

---

# Sunspot Rotation Leading to Coronal Mass Ejection

Chaowei Jiang<sup>1</sup>, Xueshang Feng<sup>1</sup>, Xinkai Bian<sup>1</sup>, Peng Zou<sup>1</sup>, Aiyong Duan<sup>2</sup>, Xiaoli Yan<sup>3</sup>, Qiang Hu<sup>4</sup>, Wen He<sup>4</sup>, Pingbing Zuo<sup>1</sup>, and Yi Wang<sup>1</sup>

<sup>1</sup>Institute of Space Science and Applied Technology, Harbin Institute of Technology, Shenzhen 518055, China

<sup>2</sup>School of Atmospheric Sciences, Sun Yat-sen University, Zhuhai 519000, China

<sup>3</sup>Yunnan Observatories, Chinese Academy of Sciences, Kunming 650216, China

<sup>4</sup>Center for Space Plasma and Aeronomic Research, The University of Alabama in Huntsville, Huntsville, AL 35899, USA

May 1, 2022

## Abstract

The rotation of sunspots around their umbral center has long been considered as an important process in driving coronal mass ejections (CMEs), but the specific mechanism remains unclear. Here with numerical magnetohydrodynamic simulations of both data-inspired and data-driven approaches, we show that the rotation of a large sunspot leads to a CME actually in a way distinct from the conventional view based on ideal instabilities of twisted flux rope. It is found that through the successive rotation of the sunspot the coronal magnetic field is sheared with a vertical current sheet created progressively, and once fast reconnection sets in the current sheet, the eruption is instantly triggered, with a highly twisted flux rope originating from the eruption. The simulations also revealed a slow-rise evolution phase sandwiched between the quasi-static energy-storage phase and the impulsive eruption-acceleration phase, and it enhances building up of the current sheet.

# 1 Introduction

Magnetic fields play a defining role for solar activities, especially, solar eruptions such as solar flares and coronal mass ejections (CMEs). The most visible manifestation of solar magnetic field are sunspots as seen on the solar surface (namely, the photosphere), which represent regions where the strongest magnetic field protrudes from the solar interior into the atmosphere. When rotating along with the solar surface, sunspots are also commonly observed to be rotating around their umbral center<sup>1;2;3;4;5</sup>, which has been discovered a century ago<sup>6;7</sup>. Such rotational motion of sunspots has long been considered as an important process in association with initiation of solar eruptions, because it is an efficient mechanism for transporting free magnetic energy and helicity from below the photosphere into the corona<sup>8;9</sup>. Indeed, almost all the flare-productive solar active regions (ARs) have been reported with significant sunspot rotations, for example, in the extensively studied ARs including NOAA 10930<sup>4;2</sup>, 11158<sup>10;11</sup>, 11429<sup>12</sup>, 12158<sup>13;14</sup>, and 12673<sup>15;16</sup>, etc.

A widely-believed physical picture on how sunspot rotation leads to CME is that the rotation can build up a magnetic flux rope (MFR, which is a bundle of magnetic flux possessing a significant amount of twist, typically characterized by a field-line twist number above unity<sup>17;18;19</sup>), and drive it into some kinds of ideal magnetohydrodynamics (MHD) instabilities<sup>20;21;22;23</sup> or catastrophic loss of equilibrium<sup>24;25;26</sup>. It seems evident that the rotational motion of magnetic field line footpoints (around the rotating center) can increase magnetic twist degree of the flux rope (around the rope axis that roots at the rotating center), until it reaches a critical value for kink instability<sup>27;28;29</sup>. Or, the flux rope will expand upward owing to the increase of magnetic pressure as driven by the rotation<sup>30</sup>, and reaches a critical height at which the torus instability<sup>20</sup> (or equivalently, the catastrophic loss of equilibrium<sup>26</sup>) sets in. However, none of these scenarios has been approved in self-consistent MHD simulations that start from a magnetic arcade and are driven by line-tied surface rotation motion. For example, all previous attempts of such type of simulations<sup>31;32;30</sup> show that the continuous twisting of the core field in a bipolar potential field can lead to a strong dynamic expansion of the field, but such dynamic expansion cannot be taken as solar eruption since there is almost no release of magnetic energy. Moreover, the twisted flux tube can always relax smoothly to an equilibrium if the driving velocities are suppressed, therefore without evidence for instability or a loss of equilibrium<sup>30</sup>. There is only one simulation<sup>33</sup> designed to show that sunspot rotation can cause the arcade overlying a pre-existing flux rope to inflate, thus weakening the confining effect on the flux rope and letting it to ascend slowly until reaching the torus instability. But in such case, it does not show how the flux rope comes into being, on the one hand, and the rotating sunspot does not play a direct role in triggering the eruption because it does not energize the key structure of eruption (i.e., the flux rope), on the other hand. Up to

65 the present, there is still no MHD simulation of solar eruption produced directly through  
66 sunspot rotation, in particular, in the realistic, complex coronal magnetic configurations.

67 Here through a comprehensive MHD simulation, with both data-constrained and data-  
68 driven approaches<sup>34</sup>, for a realistic event in solar AR NOAA 12158, we show that sunspot  
69 rotation can directly produce eruption, but the mechanism is different from any of the  
70 aforementioned ones. Our simulation shows that by applying surface rotation flow to  
71 the major sunspot, the nonpotentiality of the coronal magnetic field, as measured by the  
72 ratio of the total magnetic energy to the corresponding potential field energy, increases  
73 monotonically while the kinetic energy keeps a small value, as the MHD system evolves  
74 quasi-statically. At a critical time, there is a clear transition from the quasi-static state to  
75 an eruptive phase in which the kinetic energy impulsively rises and the magnetic energy  
76 releases quickly. Such a key transition is associated with a vertical current sheet created  
77 progressively in the sheared arcade as driven by the sunspot rotation. Once tether-cutting  
78 reconnection<sup>35</sup> sets in at the current sheet, the eruption is inevitably triggered even when  
79 we turn off the boundary driving, and a highly twisted flux rope originates from the  
80 eruption, forming a CME. This simulation also confirms a fundamental mechanism of  
81 solar eruption initiation as recently established for an idealized bipolar magnetic config-  
82 uration<sup>36</sup>.

## 83 2 Overview of the event

84 When first appearing on the solar disk, AR NOAA 12158 is already in its decaying phase,  
85 but its leading sunspot was witnessed with continuous counter-clockwise rotation for days  
86 of 6–11 September 2014 during its passage on the solar disk (Figure 1 and Supplementary  
87 Video 1). As dominated by the sunspot rotation, the coronal configuration of the AR  
88 is driven to form an inverse S-shaped structure with hot emission as seen in the Atmo-  
89 spheric Imaging Assembly (AIA) 94 Å image (Figure 1b), i.e., a sigmoid, surrounded by  
90 cooler large-scale loops as seen in AIA 171 Å (Figure 1a). To estimate the degree of its  
91 rotation with respect to the sunspot center, we calculate the surface velocity at the photo-  
92 sphere based on a time sequence of vector magnetograms, and further extract the velocity  
93 components that are directly associated with the rotational motion from the surface flow  
94 (Methods). The angular speed as averaged over three days of 8–10 September 2014 shows  
95 that the rotation is the fastest near the center of the sunspot umbra, reaching around  
96  $2.3^\circ \text{ h}^{-1}$ , and it decreases gradually to zero outside of the penumbra (Figure 1e). When  
97 averaged for the whole sunspot, the rotation speed is about  $1.75^\circ \text{ h}^{-1}$ , and thus in the  
98 three days the sunspot has rotated with a total degree of  $\sim 130^\circ$ .

99 The AR produced two major flares above Geostationary-Operational-Environmental-

100 Satellite (GOES) M class; the first one is M4.6 occurring near the end of 8 September, and  
 101 the second one is X1.6 which occurred at around 17:00 UT on 10 September. The first one  
 102 appears to be associated with no CME as seen from the LASCO onboard SOHO, while the  
 103 X1.6 flare was accompanied with a global eruption of the AR resulting in a halo CME<sup>14</sup>,  
 104 and our simulation is aimed to follow the coronal magnetic evolution leading to this major  
 105 eruption. Figure 2 (and Supplementary Video 2) shows the eruption process imaged in  
 106 three AIA channels. With about 20 min before the flare onset, a precursor is observed;  
 107 in the hot channel of AIA 131 Å, a few loops in the core of the sigmoid became more  
 108 and more prominent, while the transverse width of this brightening structure became  
 109 progressively thinner, which possibly hints that a pre-flare current sheet was forming  
 110 gradually there. Meanwhile, a set of coronal loops, likely overlying the middle part of  
 111 the sigmoid, expanded outward slowly, which looks rather faint but still detectable in  
 112 different AIA channels and can be clearly seen in the base difference images of AIA 193 Å  
 113 (Figure 2c). The speed in a direction from the flare core to the southwest is estimated  
 114 to be around 10 km s<sup>-1</sup> (Figure 3), which is at least an order of magnitude larger than a  
 115 quasi-static evolutionary speed that is driven by the photospheric motions (note that the  
 116 actual expansion speed of these loops is underestimated due to the projection effect). At  
 117 17:21 UT, the soft X-ray flux increased impulsively (Figure 3a), which indicates the onset  
 118 of fast reconnection. Instantly, the slow-expanding loops were accelerated impulsively  
 119 within about 3 min, reaching a speed of  $\sim 800$  km s<sup>-1</sup> at 17:26 UT (Figure 3b and c).  
 120 The peak value of acceleration reaches above  $\sim 10$  km s<sup>-2</sup>, which is on the same order of  
 121 magnitude of acceleration as observed in the most impulsive eruption events and is not  
 122 likely driven by an ideal MHD instability of MFR<sup>37;38</sup>. Then flare ribbons and post-flare  
 123 loops were seen with slipping-like motions, which are interpreted to be a manifestation of  
 124 3D slipping reconnection that forms an MFR during flare<sup>39;40</sup>, and a twin set of coronal  
 125 dimmings were observed in both AIA 171 and 193 Å channels along with the eruption,  
 126 which should map the feet of the erupting MFR. Although some low-lying filaments  
 127 were observed at the flare site<sup>40</sup>, they did not erupt with the flare. Previous studies of the  
 128 same event using coronal nonlinear force-free field extrapolation also suggest that only a  
 129 sheared arcade rather than a well-defined MFR existed prior to this eruption<sup>41;42</sup>.

### 130 **3 Simulation of sunspot rigid rotation leading to erup-** 131 **tion**

132 To simulate the quasi-static slow evolution of the AR until its fast eruption in a self-  
 133 consistent way, we selected 00:00 UT on 8 September 2014, a time over 65 hours before

134 onset of the X1.6 flare, as a starting point. We first constructed an MHD equilibrium  
 135 based on a single vector magnetogram taken by the Helioseismic and Magnetic Imager  
 136 (HMI) onboard the Solar Dynamics Observatory (SDO) for the starting time, using a  
 137 sophisticated MHD-relaxation technique (Methods). The MHD equilibrium represents a  
 138 snapshot of coronal evolution at that time. Then, with this well-established equilibri-  
 139 um as the initial condition, we carried out two types of MHD simulations as driven by  
 140 different surface motions specified at the bottom boundary. In the first type, which is  
 141 a data-inspired simulation, the major sunspot is rotated like a rigid body (namely with  
 142 a constant angular speed within the sunspot) while all other regions are fixed, there-  
 143 fore emphasizing the effect of sunspot rotation in leading to the eruption. In the second  
 144 type, we used directly the photospheric velocity field calculated from the time sequence  
 145 of vector magnetograms, thus being a data-driven simulation. Both types of simulation  
 146 demonstrate essentially the same evolution pattern from an initially quasi-static evolution  
 147 to finally a fast eruption, and let's focus on the first type in this section.

148 The evolutions of 3D structure of magnetic field and electric current before the eruption  
 149 are shown in Figures 4 and 5, while their evolutions during eruption are given in Figure 6,  
 150 and the time profiles of the magnetic and kinetic energies in the whole process, along with  
 151 the kinematic behaviour of the erupting features, are plotted in Figure 7. The magnetic  
 152 configuration at the initial time is a sheared arcade core enveloped by an overlying, nearly  
 153 current-free field. As the main sunspot rotates counterclockwise, the coronal magnetic  
 154 configuration expands slowly and the degree of magnetic shear increases, i.e., with the  
 155 field lines in the core part becoming more and more aligned with the bottom polarity  
 156 inversion line (PIL) as viewed from above (Figure 4a). Progressively, these field lines, as  
 157 a whole, form a prominent reverse S shape, which is also seen in the synthetic images of  
 158 coronal emission from current density (Methods) as shown in Figure 4c. It resembles the  
 159 observed coronal sigmoid structure, for example, comparing the last image of Figure 4c  
 160 with the EUV sigmoid as shown in Figure 1b. In the pre-flare phase from  $t = 0 t_s$   
 161 to  $t = 20 t_s$  (where  $t_s = 105$  s is the time unit used in the numerical model), the  
 162 magnetic energy increases monotonically with a nearly constant rate (Figure 7a), because  
 163 the sunspot rotates with a constant speed. While the magnetic energy rises significantly,  
 164 the kinetic energy keeps a small value of around  $1 \times 10^{-3} E_0$  (where  $E_0$  is the potential  
 165 field energy at the initial time), and thus most of the injected energy from the bottom  
 166 boundary through the surface driving motion (which is indicated by the gray curve in  
 167 Figure 7a) is stored as coronal magnetic energy. Moreover, since the rotation motion  
 168 introduces very limited variation to the magnetic flux distribution at the bottom surface  
 169 and thus the corresponding potential-field energy changes only slightly during the whole  
 170 evolution process, most of the injected energy is stored as free magnetic energy in the  
 171 corona. A total amount of free energy of  $\sim 0.5 E_0$  has been stored until the eruption

172 onset at  $t = 28 t_s$ , and thus the non-potentiality, as measured by the ratio of the total  
 173 magnetic energy to the potential field energy, reaches 1.9. Meanwhile, the sunspot has  
 174 rotated by about  $100^\circ$ , which is close to that derived from observations ( $\sim 110^\circ$ ), i.e., an  
 175 average rotational rate of  $1.75^\circ \text{ h}^{-1}$  (as shown in Figure 1) multiplied by a time of 65 h  
 176 before the X1.6 flare. If not interrupted by the eruption, it seems that with another  $100^\circ$   
 177 of rotation the non-potentiality can approach an upper limit of approximately 2.45 as  
 178 determined by the fully open field<sup>43;44</sup>. But such ideal evolution is not possible because  
 179 a central current sheet unavoidably forms and triggers reconnection, which results in the  
 180 eruption.

181 A clear signature of current sheet formation can be seen in the evolution of current  
 182 density in cross sections of the volume (Figure 5 and Supplementary Video 3). Note that  
 183 the current density is normalized by the magnetic field strength (i.e.,  $J/B$ ) to emphasize  
 184 thin layers with strong current. Initially the current density is volumetric, and gradually a  
 185 narrow layer with enhanced density emerges. The thickness of the current layer decreases  
 186 all the way until the onset of the eruption (see the variation of the current layer thickness  
 187 with time in Figure 7b). At the time of  $t = 28 t_s$ , the thin current layer extends from the  
 188 bottom to a height of 50 Mm with a thickness of around  $3\Delta$  (here  $\Delta = 0.72$  Mm is the  
 189 grid resolution). This is the critical time point when the current sheet reaches beyond  
 190 the grid resolution and the built-in resistivity arises to trigger fast reconnection in the  
 191 current sheet, which initiates the eruption. The current sheet formation is accompanied  
 192 with the formation of a quasi-separatrix layer (QSL<sup>45</sup>) as seen in the distribution of the  
 193 magnetic squashing degree (i.e.,  $Q$  factor, see Figure 5b and d). The  $Q$  factor quantifies  
 194 the gradient of magnetic field-line mapping with respect to their footpoints, and it is  
 195 helpful for searching topological interface or QSLs of magnetic flux connections<sup>46</sup> using  
 196 extremely large values of  $Q$  factor ( $\sim 10^5$ ). Initially the  $Q$  factor distributes smoothly  
 197 with mostly small values. Along with narrowing of the central current layer, there is an  
 198 evident increase of  $Q$  in the central thin layer. Immediately prior to the eruption, it has  
 199  $Q$  reaching  $\sim 10^5$  and an extremely small thickness, thus being identified as QSL, at the  
 200 same location with the enhanced values of  $J/B$ .

201 With onset of the eruption, the kinetic energy increases impulsively and reaches finally  
 202 about  $0.07 E_0$ , while the total magnetic energy experiences a fast decrease, even though  
 203 the boundary driving still injects magnetic energy into the volume. The total released  
 204 magnetic energy amounts to  $0.3 E_0$  or  $4 \times 10^{32}$  erg if scaled to the realistic value of the  
 205 magnetic field, which is sufficient to power a typical X-class flare<sup>47</sup>. The eruption of the  
 206 magnetic field creates a large-scale MFR through the continuous magnetic reconnection  
 207 in the current sheet (Figure 6 and Supplementary Video 4). The existence of such an  
 208 MFR in this event has been confirmed by in-situ observation in the interplanetary space  
 209 of the CME from this AR<sup>48</sup>. Ahead of the MFR, the eruption drives a fast magnetosonic

210 shock, which is shown by the thin arc of the current density on the top of the MFR.  
 211 During the eruption, the reconnecting current sheet extends in both transverse size and  
 212 height, but is kept in the same thickness that is allowed by the given grid resolution  
 213 (Figure 6). If using an sufficiently high resolution, the reconnecting current sheet would  
 214 run into plasmoid instability and could then trigger turbulence, which helps to achieve  
 215 a fast reconnection rate<sup>49;50;36</sup>. Connecting to the bottom of the current sheet is a cusp  
 216 structure, below which is the post-flare arcade, i.e., the short field lines formed after the  
 217 reconnection. The post-flare arcade and the MFR is separated, initially partially but later  
 218 fully, by the QSL that originates from the current sheet and forms the topological surface  
 219 of the MFR<sup>51</sup>. The footprints of the QSL at the bottom surface (Figure 6c) consists of  
 220 the footprints of the field lines that are undergoing reconnection in the current sheet, and  
 221 they are believed to correspond to the location of flare ribbons. Indeed, the shape and  
 222 evolution of the QSL footprints are in reasonable consistence with that of the observed  
 223 flare ribbons in SDO/AIA 1600 Å, by taking into consideration of the systematic difference  
 224 of the photospheric magnetic field between the simulation and observation. By tracing  
 225 the movement of the QSL footprints, one can compute the evolution of the reconnection  
 226 flux, which is the magnetic flux as swept by the moving QSL footprints. The results, in  
 227 both the reconnection flux and the reconnection rate, are comparable to those derived  
 228 from evolution of the observed flare ribbons<sup>52</sup> (Supplementary Figure 1).

## 229 4 The pre-eruption slow rise phase

230 Although Figure 7 shows a typical slow storage of magnetic free energy to its fast release  
 231 in eruption, the evolution can actually be divided into three different stages, that is,  
 232 a quasi-static phase, an impulsive rise phase, and a slow rise phase in between, which  
 233 can correspond to the observed short period of coronal loop slow expansion immediately  
 234 before the eruption. The first phase from the beginning to around  $t = 20 t_s$  is quasi-static  
 235 because, on the one hand, the core field expands with a speed close to that of the bottom  
 236 driving speed (Figure 7c), and on the other hand, at any instant in this phase, if we stop  
 237 the bottom driving (i.e., by turning off the rotation of the sunspot), the system can relax  
 238 smoothly to an equilibrium with gradual decline of the kinetic energy. For instance, the  
 239 kinetic energy keeps decreasing once the rotation is switched off at  $t = 20 t_s$ . In the  
 240 quasi-static phase, almost all the magnetic energy injected from the bottom boundary is  
 241 stored in the coronal volume, as shown by the close match of the energy injection line (the  
 242 gray curve in Figure 7a) and the evolution profile of the total magnetic energy. Clearly,  
 243 the time scale of the quasi-static evolution depends on that of the bottom driving. Since  
 244 we used a surface speed (of about  $10 \text{ km s}^{-1}$ ) larger than the actual photospheric motion

245 speed, the quasi-static phase in our simulation (with a duration of  $20 t_s \approx 0.6$  hours) is  
246 much shorter than the realistic one (nearly 60 hours). It can be scaled approximately to  
247 the realistic one if we use the realistic speed (for example, on the order of  $0.1 \text{ km s}^{-1}$ ) of  
248 the photospheric motion, but that demands too much computing time.

249 The second phase from around  $t = 20 t_s$  to the onset time of eruption (i.e.,  $26 t_s$ ) is a  
250 slow rise phase, in which the kinetic energy slowly rises and the magnetic energy evolution  
251 begins to deviate evidently from the magnetic energy injection curve. This phase is also  
252 featured by a relatively large speed of  $50 \sim 60 \text{ km s}^{-1}$  as shown in the expansion rate of  
253 the core field. A more important reason why this phase is different from the first phase  
254 in nature is that, if the bottom driving is turned off at any moment in this phase, the  
255 system will not relax to a static equilibrium (for example, see the evolution of the kinetic  
256 energy when the surface driving is turned off at  $t = 23 t_s$  in Figure 7a). Rather, the kinetic  
257 energy keeps an approximately constant value without decay, and meanwhile the magnetic  
258 energy decreases slowly. Moreover, no matter at which moment the boundary driving is  
259 switched off, the system will always reach an eruption phase after a short interval of  
260 evolution (for instance, see the case with sunspot rotation stopped at  $t = 23 t_s$ , for which  
261 the magnetic field and current density evolution are shown in Supplementary Video 5).  
262 These experiments show that the bottom driving is not necessary in maintaining the slow  
263 rise phase (once it begins), although it can slightly speed up this process. This indicates  
264 that the slow rise phase is a self-maintained non-equilibrium (but stable) and therefore its  
265 timescale of evolution is inherent to the dynamics in the corona rather than determined  
266 by the bottom driving speed. The time duration of slow rise phase is around  $6 t_s$ , which  
267 is on the same order of that of the observed slow rise phase (around 20 min).

268 Why the slow rise phase must proceed nearly the same time before the eruption,  
269 regardless of the bottom boundary driving? This is because the current sheet must reach  
270 the critical thickness can then the eruption be triggered by reconnection. In Figure 7b,  
271 we also show evolution of the thickness of the current sheet in the different runs. As  
272 can be seen, the current layer is continually thinned and once its thickness is below the  
273 resolvable limit of the grid resolution (about 3 grid sizes), the impulsive acceleration of the  
274 fast eruption phase begins. When turning off the bottom driving at  $t = 23 t_s$ , the current  
275 layer is still thinned although the rate is slightly slower, and the eruption is initiated in  
276 the same way when the current sheet reaches the critical thickness. In contrast, when the  
277 boundary driving is stopped at  $t = 20 t_s$  before the slow-rise phase begins, the system  
278 will relax to an equilibrium without changing the thickness of the current layer, and thus  
279 cannot develop the current sheet as required for reconnection.

## 5 Data-driven simulation leading to eruption

As the second type of simulation, we first derived the surface plasma flow at the photosphere and then input the velocity into the MHD model as a data-driven boundary condition. Since the AR shows no flux emergence during the studied period, and the sunspot rotation is reflected only in the horizontal motion, we only use the horizontal flows to drive the model. Furthermore, observations show that there is a large amount (around 30%) of flux decrease in the three days due to persistent flux dispersion and diffusion associated with the decaying of the AR, we used an enhanced surface diffusion term to the magnetic field at the bottom boundary (see details in Methods), which on the one hand can simulate the overall flux decrease, and on the other hand can avoid over steepening of magnetic flux density at the moat of the sunspot. Otherwise in the simulation the magnetic flux as carried outward persistently by the diverging moat flows will pileup at the locations where the moat flows disappear. It should be noted that the boundary conditions in our data-driven model as driven by the derived photospheric flow field do not reproduce exactly the time-varying observed magnetograms at the bottom boundary (Methods).

Results of this data-driven simulation are shown in Figure 8 for evolution of magnetic field and current density before the eruption, in Figure 9 for during eruption (and Supplementary Video 6), and in Figure 10 for the temporal variation of magnetic flux, various types of energies, and the thickness of the current layer. The structure and evolution are essentially similar to the results of the simulation with sunspot rigid rotation, regarding to the formation of the sigmoid, the current sheet, as well as the erupting twisted MFR. This similarity of evolution demonstrated the robustness of the fundamental mechanism of eruption initiation. A notable difference between this simulation and the previous one is that, here both the total and potential magnetic energies decay gradually (Figure 10b), owing to the decrease of the total magnetic flux. Nevertheless, the free magnetic energy shows a continuous increase before the eruption and experiences a fast decrease during the eruption. This evolution pattern is clearer in the profile of the ratio of total magnetic energy to the potential field energy, i.e., the non-potentiality. It first increases monotonically to a critical value of 1.9, and then decreases with the onset of the eruption, which is strikingly similar to that of the previous simulation. Another noticeable point is that the timing of the simulation coincides well with the observed evolution; the onset time of the observed flare is at  $t = 65$  h, which corresponds rather well to the simulated eruption start time of near  $t = 32 t_s$ , by considering that the boundary driving is sped up by 68.6 times (thus in the quasi-static driving phase,  $t_s$  corresponds to 2 hours, see Methods). During the eruption, the evolution speed is determined by the corona itself, so the interval from the eruption onset time to the peak time of kinetic energy is around  $14 t_s$  (24 min), and

317 this matches closely the observed duration from the GOES flare onset time to its peak  
318 time, which is also 24 min.

## 319 6 Discussion

320 Our simulations, in both the data-inspired and data-driven approaches, demonstrated that  
321 the continuous rotation of a major sunspot of an AR leads to a CME in a way distinct  
322 from the conventional view based on ideal MHD instabilities of twisted flux rope. It is  
323 found that through the successive rotation of the sunspot the coronal field is sheared with  
324 a vertical current sheet created progressively, and once fast reconnection sets in at the  
325 current sheet, the eruption is instantly triggered, and a highly twisted flux rope originates  
326 from the eruption, forming a CME. The simulations also revealed explicitly a slow-rise  
327 evolution phase between the quasi-static phase of non-potential magnetic energy storage  
328 and the impulsive acceleration phase of eruption. Such a slow-rise phase is commonly  
329 observed in many eruption events (including the studied one) for either erupting fila-  
330 ments or coronal loops but still lacks a physical explanation. Our analysis suggests that  
331 the slow-rise phase is a coronal self-maintained, non-equilibrium but stable, evolutionary  
332 state inherent to the coronal dynamics rather than controlled by the photospheric driving  
333 motions as considered before<sup>53</sup>. Once began, the slow-rise phase will develop for a short  
334 time interval (often with a few tens of minutes), even the boundary driving is turned off,  
335 and eventually transfers into the final eruption. This short phase plays an important role  
336 in building up of the current sheet, since it accelerates the thinning of the current layer  
337 that is built up in the quasi-static phase until the reconnection sets in.

338 Why do the realistic simulations support such a scenario rather than that based on  
339 MHD instabilities of pre-eruption MFRs? There are two reasons. Firstly, the rotation of  
340 sunspot is too slow to form a well-defined MFR in a few days. Observations show that  
341 the angular rotational speed for many sunspots is on average a few degrees per hour and  
342 the total rotation degree is mostly between 40–200° over periods of 3–5 days<sup>1</sup>. Thus,  
343 the resulted magnetic twist by such rotation is far lower than that necessary to form a  
344 well-defined MFR (which needs field lines winding around an axis with at least one turn,  
345 or twist of 360°) and further to trigger the ideal kink instability (which needs winding  
346 number of more than 1.25 turns<sup>27</sup> or twist of more than 450°). Even though there is a  
347 sunspot (for example in the AR 10930) reported to rotate by a large amount of about  
348 500° over five days<sup>4</sup>, there are many eruptions in the duration (AR 10930 produced 4  
349 X-class eruptive flares and a few smaller ones) and thus these eruptions should release  
350 substantially the built-up twist repeatedly, preventing the continuous formation of a highly  
351 twisted rope. Furthermore, the origin of sunspot rotation is believed to be a consequence

352 of the emergence of twisted magnetic flux tube, as created in the solar interior, into the  
353 corona<sup>54;55;56</sup>. As shown by many numerical simulations of flux emergence<sup>57</sup>, the twisted  
354 flux tube cannot rise bodily from below the photosphere, and the twist of tube in the  
355 convection zone is partially transferred into the corona through a torsional Alfvén wave  
356 propagated along the tube, while the sunspot rotation is a manifestation of this twist-  
357 transferring process<sup>57</sup>. All these facts suggest that MFR is not easy to be created by flux  
358 emergence and its resultant sunspot rotation alone.

359 Secondly, sunspot rotation, although slow, is a very efficient way of injecting magnetic  
360 free energy. For example, by modelling of a solar flare from 13 May 2005, it has been  
361 shown that the sunspot rotation of the source AR dominates the energy accumulation  
362 for the flare event<sup>58</sup>. In fact, such sunspot rotation alone can store sufficient energy to  
363 power a very large flare. Our simulation demonstrated this point more clearly as shown  
364 in Figure 7a; by a rotation of  $90^\circ$  (on average for the whole sunspot), the free energy has  
365 been increased by over 50% of the potential field energy. As the open field energy is an  
366 upper limiter, which is around 2.5 times of the potential field energy, this made it very  
367 easy for the field to reach the open field energy, if the rotation is as large as  $300^\circ$ . The  
368 open field is closely related to the building up of the current sheet, since a current sheet  
369 must be built up before the field becoming fully open, as consistent with our previous  
370 high-resolution simulation based on a simple bipolar field<sup>36</sup>. Thus, to build up a current  
371 sheet needs much less degree of rotation than that for building up an unstable MFR, as  
372 the former is more consistent with the observation of the rotation degrees.

373 Nevertheless, there is also a possibility in some events that the rotation of sunspot  
374 drives the formation of the current sheet, but a confined flare is resulted if the overlying  
375 field is strong enough (or decay slowly enough) to constrain the newly-formed, erupting  
376 flux rope. With continuous rotation, such confined flares might occur multiple times  
377 and jointly build up an ideal unstable MFR that eventually erupts, as suggested by  
378 recent observations<sup>5</sup>. This will need further investigations with future data-driven MHD  
379 simulations<sup>34</sup>.

## 380 Methods

### 381 Model equations

382 The simulation is carried out by solving numerically the MHD equations as follows, using  
 383 an advanced conservation element and solution element (CESE) method<sup>59;60</sup>,

$$\begin{aligned}
 \frac{\partial \rho}{\partial t} + \nabla \cdot (\rho \mathbf{v}) &= -\nu_\rho (\rho - \rho_0), \\
 \rho \frac{d\mathbf{v}}{dt} &= -\nabla p + \mathbf{J} \times \mathbf{B} + \rho \mathbf{g} + \nabla \cdot (\nu \rho \nabla \mathbf{v}), \\
 \frac{\partial \mathbf{B}}{\partial t} &= \nabla \times (\mathbf{v} \times \mathbf{B}), \\
 \frac{\partial T}{\partial t} + \nabla \cdot (T \mathbf{v}) &= (2 - \gamma) T \nabla \cdot \mathbf{v}.
 \end{aligned} \tag{1}$$

384 where the electric current density  $\mathbf{J} = \nabla \times \mathbf{B}$ ,  $\nu$  is the kinetic viscosity, and  $\gamma$  is the  
 385 adiabatic index. Note that the equations are written in non-dimensionalized form with  
 386 all variables normalized by their typical values at the base of the corona, which are,  
 387 respectively, density  $\rho_s = 2.29 \times 10^{-15} \text{ g cm}^{-3}$ , temperature  $T_s = 10^6 \text{ K}$ , velocity  $v_s =$   
 388  $110 \text{ km s}^{-1}$ , magnetic field  $B_s = 1.86 \text{ G}$ , length  $L_s = 11.52 \text{ Mm}$ , and time  $t_s = 105 \text{ s}$ .

In this simulation, an artificial source term  $-\nu_\rho(\rho - \rho_0)$  has been added to the continuity equation (i.e., the first equation in Equations (1), where  $\rho_0$  is the density at the initial time  $t = 0$ , and  $\nu_\rho$  is a prescribed coefficient given as  $\nu_\rho = 0.05 v_A$  ( $v_A = B/\sqrt{\rho}$  is the Alfvén speed). This term is used to avoid ever decreasing of the density in the strong magnetic field region, an issue often encountered in simulations handling very large magnetic field gradients and at the same time with very low plasma  $\beta$ <sup>61</sup>. It can maintain the maximum Alfvén speed in a reasonable level, which may otherwise increase and make the iteration time step smaller and smaller and the long-term simulation unmanageable. This source term is actually a Newton relaxation of the density to its initial value by a time scale of

$$\tau_\rho = \frac{1}{\nu_\rho} = 20\tau_A, \tag{2}$$

389 where  $\tau_A = 1/v_A$  is the Alfvén time with length of 1 (the length unit  $L_s$ ). Thus it is  
 390 sufficiently large to avoid influence on the fast dynamics of Alfvénic time scales.

391 Similar to our previous works<sup>36;61</sup>, we chose to not use explicit resistivity in the magnet-  
 392 ic induction equation, but magnetic reconnection can still be triggered through numerical  
 393 diffusion when a current layer is sufficiently narrow with thickness close to the grid reso-  
 394 lution. By this, we achieved an effective resistivity as small as we can with a given grid

395 resolution, and also mimicked the current-density-dependent resistivity as required for  
 396 fast Petscheck-type reconnection. For simplicity, the adiabatic index is set as  $\gamma = 1$  in the  
 397 energy (or temperature) equation, which thus reduces to an isothermal process. Although  
 398 in this case we can simply discard the energy equation by setting the temperature as a  
 399 constant, we still keep the full set of equations in our code and can thus describe either the  
 400 isothermal or adiabatic process by choosing particular values of  $\gamma$ . The kinetic viscosity  
 401  $\nu$  is given with different values when needed, which is described in the following sections.

## 402 Construction of an initial MHD equilibrium

403 To initialize the surface flow-driven simulations, an MHD equilibrium is constructed based  
 404 on the SDO/HMI vector magnetogram taken for time of 00:00 UT on 8 September 2014.  
 405 Such an equilibrium is assumed to exist when the corona is not in the eruptive stage,  
 406 and is crucial for starting our subsequent surface flow-driven evolution. Beforehand we  
 407 preprocessed the vector magnetogram use a method developed in ref.<sup>62</sup> and further s-  
 408 smoothed all the three components of the magnetic field using Gaussian smoothing with  
 409 FWHM of 6 arcsec. This is done for two reasons: on the one hand, the preprocessing  
 410 minimizes the photospheric Lorentz force contained in the vector magnetogram, which is  
 411 helpful for reaching a more force-free equilibrium state<sup>63</sup>; on the other hand, the smooth-  
 412 ing effectively filters out the small-scale magnetic structures that cannot be sufficiently  
 413 resolved in our simulation, and it also mimics the effect of magnetic field expansion from  
 414 the photosphere to the base of the corona<sup>64</sup>, since the lower boundary of our simulation  
 415 is assumed to be the coronal base rather than directly the photosphere<sup>65;66</sup>.

416 We constructed the MHD equilibrium based on an MHD-relaxation approach consist-  
 417 ing of two steps<sup>61</sup>. In the first step, a potential magnetic field  $\mathbf{B}_{\text{pot}}$  extrapolated from  
 418 the vertical component (i.e.,  $\mathcal{B}_z$ ) of the preprocessed and smoothed vector magnetogram  
 419  $(\mathcal{B}_x, \mathcal{B}_y, \mathcal{B}_z)$ , along with an initial plasma as the background atmosphere were input in-  
 420 to the MHD model. For the initial plasma, we used an isothermal gas in hydrostatic  
 421 equilibrium. It is stratified by solar gravity with a density  $\rho = 1$  at the bottom and a  
 422 uniform temperature of  $T = 1$ . With the plasma configured by typical coronal density  
 423 and temperature, we chose to reduce the original magnetic field strength by a factor of 20,  
 424 such that the maximum of magnetic field strength in normalized value is approximately  
 425  $50 \sim 100$  in the model. If using the original values of magnetic field, its strength (and  
 426 the characteristic Alfvén speed) near the lower surface is too large, and will put a too  
 427 heavy burden on computation since the time step of our simulation is limited by the CFL  
 428 condition.

429 With these initial conditions, we modified the transverse magnetic fields on the bottom  
 430 boundary incrementally in time (using linear extrapolation with a duration of  $t = 1$ ) from

431 that of the potential field  $\mathbf{B}_{\text{pot}}$  to that of the vector magnetogram  $(\mathcal{B}_x, \mathcal{B}_y, \mathcal{B}_z)$ . The process  
432 drives the coronal magnetic field to evolve away from the initial potential state, since the  
433 change of the transverse field injects electric currents and thus Lorentz forces, which induce  
434 motions in the computational volume. In this phase all other variables on the bottom  
435 boundary are simply fixed, thus the plasma remains to be motionless there. Although  
436 this procedure is somewhat un-physical since the Lorentz force will also introduce nonzero  
437 flows on the bottom boundary, it provides a simple and ‘safe’ way (avoiding numerical  
438 instability) to bring the transverse magnetic field into the MHD model. Once the magnetic  
439 field on the bottom surface is identical to that of  $(\mathcal{B}_x, \mathcal{B}_y, \mathcal{B}_z)$ , the MHD system is then  
440 allowed to relax to an equilibrium with all the variables (including the magnetic field)  
441 on the bottom boundary fixed. To avoid a too large velocity in this phase such that the  
442 system can relax fast, we set a relatively large kinetic viscosity coefficient, which is given  
443 by  $\nu = 0.5\Delta x^2/\Delta t$  (where  $\Delta x$  is the local grid spacing and  $\Delta t$  the local time step as  
444 determined by the CFL condition with the fastest magnetosonic speed). Actually this  
445 is the largest viscosity one can use with a given grid size  $\Delta x$  and time step  $\Delta t$ , because  
446 the CFL condition for a purely diffusive equation with diffusion coefficient  $\nu$  requires  
447  $\Delta t \leq 0.5\Delta x^2/\nu$ . The relaxation phase takes a time of  $t = 20$  with the average relative  
448 residual of magnetic field in the whole volume between two consecutive time steps reduced  
449 to a sufficiently small level of below  $10^{-5}$ .

In the second step, we carried out a ‘deeper’ relaxation by running the model again  
but started with the relaxed magnetic field obtained in the first step and the initially  
hydrostatic plasma. We reduced the kinetic viscosity to  $\nu = 0.05\Delta x^2/\Delta t$ , i.e., an order  
of magnitude smaller than that used in the first step, which corresponds to a Reynolds  
number of 10 for the length of a grid cell  $\Delta x$ . Furthermore, the magnetic field at the  
bottom boundary is allowed to evolve in a self-consistent way with assumptions that the  
bottom boundary is a perfectly line-tying and fixed (i.e.,  $\mathbf{v} = 0$ ) surface of magnetic  
field lines. Note that such a line-tying condition does not indicate that all magnetic field  
components on the boundary are fixed, because even though the velocity  $\mathbf{v}$  is given as  
zero on the bottom boundary, it is not necessarily zero in the neighboring inner points.  
To self-consistently update the magnetic field, we solve the magnetic induction equation  
on the bottom boundary. Slightly different from the one in the main equations (1), the  
induction equation at the bottom surface is given by

$$\frac{\partial \mathbf{B}}{\partial t} = \nabla \times (\mathbf{v} \times \mathbf{B}) + \eta_p \nabla_{\perp}^2 \mathbf{B}, \quad (3)$$

450 where we added a surface diffusion term defined by a surface Laplace operator as  $\nabla_{\perp}^2 =$   
451  $\frac{\partial^2}{\partial x^2} + \frac{\partial^2}{\partial y^2}$  with a small resistivity for numerical stability near the PIL  $\eta_p = 1 \times 10^{-3} e^{-B_z^2}$ ,  
452 since the photospheric magnetic fields often have the strongest gradient across the main

453 PIL. The surface induction Equation (3) in the code is realized by second-order difference  
 454 in space and first-order forward difference in time. Specifically, on the bottom boundary  
 455 (we do not use ghost cell), we first compute  $\mathbf{v} \times \mathbf{B}$ , and then use central difference in  
 456 horizontal direction and one-sided difference (also 2nd order) in the vertical direction to  
 457 compute the convection term  $\nabla \times (\mathbf{v} \times \mathbf{B})$ . The surface Laplace operator is also realized  
 458 by central difference.

459 Supplementary Figure 2a and b shows the 3D magnetic field lines of the final relaxed  
 460 MHD equilibrium, which has a small ratio of kinetic energy to magnetic energy of below  
 461  $10^{-3}$ . Note that the field lines are pseudo-colored by the values of the force-free factor  
 462 defined as  $\alpha = \mathbf{J} \cdot \mathbf{B}/B^2$ , which indicates how much the field lines are non-potential. For  
 463 a force-free field, this parameter is constant along any given field line. As can be seen,  
 464 the magnetic field is close to a force-free one since the color is nearly the same along any  
 465 single field line. In the core of the configuration, the field lines are sheared significantly  
 466 along the PIL, thus having large values of  $\alpha$  and current density. On the other hand,  
 467 the overlying field is almost current-free or quasi-potential field with  $\alpha \sim 0$ , and it plays  
 468 the role of strapping field that confines the inner sheared core. Supplementary Figure 2c  
 469 shows the profile of plasma  $\beta$  and Alfvén speed with height, as an example, along a  
 470 vertical line with footpoint at the center of the main sunspot. The largest Alfvén speed is  
 471 more than  $6 \times 10^3 \text{ km s}^{-1}$ , and the plasma  $\beta$  is mostly smaller than unity below 300 Mm  
 472 with the smallest value of  $5 \times 10^{-4}$ , therefore characterizing well the essential conditions  
 473 of dynamics in the corona, i.e., very large Alfvén speed and low plasma  $\beta$ .

## 474 Rigid rotation of the sunspot

The surface rigid rotation of the sunspot with respect to its surrounding field is applied  
 with a velocity profile defined by

$$v_x = -\omega(y - y_c), \quad v_y = \omega(x - x_c) \quad (4)$$

475 where the rotating center  $(x_c, y_c)$  is defined to be a point in the sunspot with the largest  
 476  $B_z$ , and the angular speed  $\omega$  is a constant (positive, thus rotating counter-clockwise)  
 477 within a radius of 10 arcsec from the rotating center, and then decreases linearly to zero  
 478 at a radius of 35 arcsec. The value of  $\omega$  is scaled such that the maximum value of the  
 479 surface speed is  $10 \text{ km s}^{-1}$ . Supplementary Figure 2d shows the distribution of the surface  
 480 flow. The implementation of the bottom boundary conditions is the same as that for the  
 481 second step (the deeper relaxation phase) described in ‘Construction of an initial MHD  
 482 equilibrium’. That is, on the bottom surface, we solved the Equation (3) to update all  
 483 the three components of magnetic field with the flow field prescribed by those defined in  
 484 Equation (4), while the plasma density and temperature are simply fixed.

## 485 Photospheric velocity recovering and data-driven simulation

486 Without a direct observation, the surface velocity at the photosphere is often derived  
487 from the time series data of vector magnetograms, and we used such a velocity-recovering  
488 method called DAVE4VM<sup>67</sup>. It is a differential affine velocity estimator (DAVE) designed  
489 for vector magnetogram (VM), which uses a variational principle to minimize statistically  
490 deviations in the magnitude of the magnetic induction equation. The vector magne-  
491 tograms are provide by the SDO/HMI SHARP data with cadence of 12 minutes and pixel  
492 size of 1 arcsec (by rebinning the original data with pixel size of 0.5 arcsec). Since there  
493 are a few time gaps in our studied time interval, we first filled the data gap using linear  
494 interpolation in the time domain to generate a complete time series from 00:00 UT on 8  
495 September 2014 to 24:00 UT on 10 September 2014. Then we input the time series of  
496 vector magnetogram into the DAVE4VM code. We set the window size of sampling, a  
497 key parameter in the DAVE4VM code, as its optimized value of 19 pixels<sup>68:69</sup>.

498 After obtaining the surface velocity, we made a correction by removing the velocity  
499 component parallel to the magnetic field, since this field-aligned velocity is artificial and  
500 makes no contribution in the magnetic induction equation. To reduce the data noises,  
501 the time series of flow maps are smoothed in both the time and space domains, with a  
502 Gaussian FWHM of 2 hours for time (i.e., 10 times of the data cadence) and 6 arcsec for  
503 both  $x$  and  $y$  directions, respectively, and are finally entered into the data-driven model.  
504 Figure 1d shows a snapshot of the surface velocity after this smoothing. The speed of the  
505 flow is generally a few hundreds of meters per second and the main feature is a clear and  
506 persistent rotation of the main sunspot. Note that during the three days the basic config-  
507 uration of the photospheric magnetic flux distribution is rather similar with only gradual  
508 dispersion as small magnetic flux fragments, known as moving magnetic features<sup>70</sup>, move  
509 outward from the sunspots as advected by the moat flow (i.e., the diverging flow existing  
510 persistently in the periphery of the sunspot). So the magnetic energy injection should  
511 come mainly from the transverse rotational flows.

512 Here to save computing time, the cadence of the input flow maps, which is originally  
513 12 min, was increased by 68.6 times when inputting into the MHD model. This means  
514 that a unit of time in the simulation,  $t_s$ , corresponds to actually  $t_s \times 68.6 = 7200$  s, i.e., 2  
515 hours, in the HMI data. Compressing of the time in HMI data is justified by the fact that  
516 the speed of photospheric flows is often a few of  $10^2$  m s<sup>-1</sup>. So in our model settings, the  
517 evolution speed of the boundary field, even enhanced by a factor of 68.6, is still smaller by  
518 two orders of magnitude than the coronal Alfvén speed (on the order of  $10^3$  km s<sup>-1</sup>), and  
519 the quick reaction of the coronal field to the slow bottom changes should not be affected.

The implementation of the bottom boundary conditions is the same as that for the  
simulation driven by sunspot rigid rotation, except that here an enhanced surface diffusion

of magnetic field dependent on the local field strength is applied by

$$\eta_p = 2 \times 10^{-3} + \begin{cases} \left(\frac{B}{100}\right)^2 \times 10^{-2} & ; B \leq 100 \\ 10^{-2} & ; B \geq 100 \end{cases} \quad (5)$$

520 Such an enhanced diffusion term is used mainly to avoid a too large magnetic flux density  
521 accumulated at the moat of the sunspot.

522 It should be noted that the data-driven simulation cannot reproduce exactly the evolu-  
523 tion of the photospheric magnetic field (in its three components) for mainly two reasons.  
524 The first one is the omission of the vertical component of the photospheric velocity in  
525 the simulation. The second one is the inherent limitation of the DAVE4VM code and  
526 also similar flow tracking methods, since the derived velocity (along with the magnetic  
527 field) only approximately satisfies the vertical component of the magnetic induction equa-  
528 tion, and moreover the equation is used in a statistical way rather than a point-by-point  
529 sense<sup>67</sup>.

## 530 Grid setting and numerical boundary conditions

531 For the purpose of minimizing the influences introduced by the side and top numerical  
532 boundaries of the computational volume, we used a sufficiently large box of  $(-32, -32, 0) <$   
533  $(x, y, z) < (32, 32, 64)$  embedding the field of view of the magnetogram of  $(-8.75, -8.25) <$   
534  $(x, y) < (8.75, 8.25)$ . The full computational volume is resolve by a non-uniform block-  
535 structured grid with adaptive mesh refinement (AMR), in which the highest and lowest  
536 resolution are  $\Delta x = \Delta y = \Delta z = 1/16$  (corresponding to 1 arcsec or 720 km, matching  
537 the resolution of the vector magnetogram) and  $1/2$ , respectively. The AMR is controlled  
538 to resolve with the smallest grids the regions of strong magnetic gradients and current  
539 density, particularly near the current sheet. The magnetic field outside of the area of  
540 the magnetograms on the lower boundary is given as zero for the vertical component  
541 and simply fixed as the potential field for the transverse components. On the side and  
542 top boundaries, we fixed the plasma density, temperature, and velocity. The horizontal  
543 components of magnetic field are linearly extrapolated from the inner points, while the  
544 normal component is modified according to the divergence-free condition to avoid numer-  
545 ical errors of magnetic divergence accumulated on these boundaries. Furthermore, the  
546 simulation runs are stopped before the disturbance by the eruption reaches any of these  
547 boundaries to minimize the influence of these numerical boundaries on the computation.

548 **Estimation of sunspot rotation**

Based on the photospheric surface velocity as derived, the rotational speed is estimated in the following way. We first extract the velocity components relevant only to the rotational motion from the surface horizontal velocity  $\mathbf{v}$  by decomposing it as

$$\mathbf{v} = \mathbf{v}_1 + \mathbf{v}_2 = \nabla \times \mathbf{p} + \nabla q, \quad (6)$$

where the curl-free part  $\mathbf{v}_2 = \nabla q$  is obtained by solving a Poisson equation  $\nabla^2 q = \nabla \cdot \mathbf{v}$ , and then the divergence-free part is  $\mathbf{v}_1 = \nabla \times \mathbf{p} = \mathbf{v} - \mathbf{v}_2$ . The rotational flow of the sunspot is contained only in the divergence-free field  $\mathbf{v}_1$ . Then we estimated the time average of the rotational flow of three days by simply averaging the field  $\mathbf{v}_1$  in each pixel using the three-day data of 8–10 September 2014. Supplementary Figure 3a gives the distribution of the averaged  $\mathbf{v}_1$ . As can be seen, the rotating center is close to the location with the maximum magnetic flux density in the sunspot (also on time average). With this averaged flow field, we further calculated the rotational rate, i.e., the angular speed of the sunspot with respect to the rotating center. As shown in Supplementary Figure 3b, we sampled in total 100 radial lines with different azimuthal angle  $\phi$  (evenly distributed from 0 to  $2\pi$ ) from the center of rotation, and got the rotational velocity  $v_\phi(r, \phi)$  on these radial lines. Then the average angular speed is

$$\omega(r) = \frac{1}{2\pi} \int \frac{v_\phi(r, \phi)}{r} d\phi, \quad (7)$$

549 which shows that the angular speed is largest with value of  $2.5^\circ \text{ h}^{-1}$  in the rotation center,  
 550 and gradually decreases to zero at a radial distance of 25 Mm. Our result of the total  
 551 rotation degree for the three days from 8–10 September 2014 agrees well with the value  
 552 obtained from other independent methods for the same sunspot<sup>71;14</sup>.

553 **Synthetic images of coronal emission from current density**

554 The synthetic images of coronal EUV emission are generated using a method similar to  
 555 that proposed in ref<sup>72</sup>. Since it is commonly believed that the coronal loops generally  
 556 reflect the structure of the magnetic field lines rooted in the photosphere, we first traced  
 557 a sufficiently large number ( $\sim 10^6$ ) of field lines with their footpoints uniformly distributed  
 558 at the bottom surface. All the field lines are traced with fixed step of 720 km. Then on  
 559 each field line, all the line segments are assigned with a proxy value of emission intensity  
 560 represented by the averaged square of current density along this field line, by simply  
 561 assuming that the Ohmic dissipation of the currents heats the corona. Finally, the total

562 emission along the line of sight (here simply along the  $z$  axis) is obtained by integrating  
563 all the emission intensity along the  $z$  axis, which forms the final synthetic image.

564

565 **Correspondence and requests for materials** should be addressed to C.W.J. ([chaowei@hit.edu.cn](mailto:chaowei@hit.edu.cn))  
566 and X.S.F. ([fengx@spaceweather.ac.cn](mailto:fengx@spaceweather.ac.cn))

567

568 **Acknowledgments.** C.W.J. acknowledges support from National Natural Science Foun-  
569 dation of China (NSFC) grants 42174200 and 41731067, the Fundamental Research Funds  
570 for the Central Universities (Grant No. HIT.OCEF.2021033), and the Shenzhen Sci-  
571 ence and Technology Program (RCJC20210609104422048 and JCYJ20190806142609035).  
572 X.S.F. is supported by NSFC grants 42030204, 41861164026 and 41874202 and the S-  
573 trategic Priority Program of the Chinese Academy of Sciences, Grant No. XDB41000000.  
574 X.L.Y. is supported by NSFC grant 11873087, Yunnan Science Foundation for Distingu-  
575 guished Young Scholars under No. 202001AV070004. Data from observations are cour-  
576 tesy of NASA SDO. The computational work was carried out on TianHe-1(A), National  
577 Supercomputer Center in Tianjin, China.

578

579 **Author contributions.** C.W.J. conceived the study, developed the numerical MHD  
580 model, performed the result analysis and wrote the text. X.S.F. contributed to the design  
581 of numerical MHD schemes. X.K.B. contributed to the computation of the magnetic en-  
582 ergies and the synthetic image of coronal emission. All authors participated in discussions  
583 and revisions on the manuscript.

584

585 **Competing financial interests.** The authors declare no competing financial interests.

586

587 **Data availability.** All SDO data are publicly available at <http://jsoc.stanford.edu/ajax/lookdata>.  
588 The data generated by the 3D MHD simulations and analyzed for this paper occupy a  
589 large amount and interested parties are invited to contact the corresponding authors to  
590 make arrangements for the transfer of those data.

591

592 **Code availability.** We have opted not to make our numerical code of the MHD simula-  
593 tion publicly available owing to its complexity, which demands expert assistance to set up,  
594 run and analyze simulations, and because it is continually being improved and extended,  
595 which requires frequent software updates. Interested parties are invited to contact the  
596 authors for more detailed information.

## References

- 597
- 598 [1] Brown, D. *et al.* Observations of Rotating Sunspots from TRACE. *Solar Physics*  
599 **216**, 79–108 (2003).
- 600 [2] Zhang, J., Li, L. & Song, Q. Interaction between a Fast Rotating Sunspot and  
601 Ephemeral Regions as the Origin of the Major Solar Event on 2006 December 13.  
602 *The Astrophysical Journal* **662**, L35–L38 (2007).
- 603 [3] Yan, X.-L., Qu, Z.-Q. & Kong, D.-F. Relationship between rotating sunspots and  
604 flare productivity. *Monthly Notices of the Royal Astronomical Society* **391**, 1887–  
605 1892 (2008).
- 606 [4] Min, S. & Chae, J. The Rotating Sunspot in AR 10930. *Solar Physics* **258**, 203–217  
607 (2009).
- 608 [5] James, A. W., Green, L. M., van Driel-Gesztelyi, L. & Valori, G. A new trigger  
609 mechanism for coronal mass ejections. The role of confined flares and photospheric  
610 motions in the formation of hot flux ropes. *Astronomy & Astrophysics* (2020).
- 611 [6] Evershed., J. Radial Movement in Sun-spots. (Second Paper.). *Monthly Notices of*  
612 *the Royal Astronomical Society* **70**, 217–226 (1910).
- 613 [7] St. John, C. E. Radial Motion in Sun-Spots. *The Astrophysical Journal* **37**, 322  
614 (1913).
- 615 [8] Stenflo, J. O. A mechanism for the build-up of flare energy. *Solar Physics* **8**, 115–118  
616 (1969).
- 617 [9] Barnes, C. W. & Sturrock, P. A. Force-Free Magnetic-Field Structures and Their  
618 Role in Solar Activity. *The Astrophysical Journal* **174**, 659 (1972).
- 619 [10] Jiang, Y. *et al.* RAPID SUNSPOT ROTATION ASSOCIATED WITH THE X2.2  
620 FLARE ON 2011 FEBRUARY 15. *The Astrophysical Journal* **744**, 50 (2012).
- 621 [11] Vemareddy, P., Ambastha, A. & Maurya, R. A. ON THE ROLE OF ROTATING  
622 SUNSPOTS IN THE ACTIVITY OF SOLAR ACTIVE REGION NOAA 11158. *The*  
623 *Astrophysical Journal* **761**, 60 (2012).
- 624 [12] Zheng, J. *et al.* Sunspots rotation and magnetic transients associated with flares  
625 in NOAA AR 11429. *Research in Astronomy and Astrophysics* **17**, 081 (2017).  
626 [1704.08018](https://doi.org/10.1088/1751-0858/17/08/08018).

- 627 [13] Bi, Y. *et al.* Observation of a reversal of rotation in a sunspot during a solar flare.  
628 *Nature Communications* **7**, 13798 (2016).
- 629 [14] Vemareddy, P., Cheng, X. & Ravindra, B. SUNSPOT ROTATION AS A DRIVER  
630 OF MAJOR SOLAR ERUPTIONS IN THE NOAA ACTIVE REGION 12158. *The*  
631 *Astrophysical Journal* **829**, 24 (2016).
- 632 [15] Yan, X. L. *et al.* Simultaneous Observation of a Flux Rope Eruption and Magnetic  
633 Reconnection during an X-class Solar Flare. *The Astrophysical Journal* **853**, L18  
634 (2018).
- 635 [16] Yan, X. L. *et al.* Successive X-class Flares and Coronal Mass Ejections Driven by  
636 Shearing Motion and Sunspot Rotation in Active Region NOAA 12673. *The Astro-*  
637 *physical Journal* **856**, 79 (2018).
- 638 [17] Chen, J. Physics of erupting solar flux ropes: Coronal mass ejections  
639 (CMEs)—Recent advances in theory and observation. *Physics of Plasmas* **24**, 090501  
640 (2017).
- 641 [18] Cheng, X., Guo, Y. & Ding, M. Origin and structures of solar eruptions I: Magnetic  
642 flux rope. *Science China Earth Sciences* **60**, 1383–1407 (2017).
- 643 [19] Liu, R. Magnetic flux ropes in the solar corona: Structure and evolution toward  
644 eruption. *Research in Astronomy and Astrophysics* **20**, 165 (2020).
- 645 [20] Kliem, B. & Török, T. Torus Instability. *Physical Review Letters* **96**, 255002 (2006).
- 646 [21] Török, T. & Kliem, B. Confined and Ejective Eruptions of Kink-unstable Flux Ropes.  
647 *The Astrophysical Journal* **630**, L97–L100 (2005).
- 648 [22] Fan, Y. & Gibson, S. E. Onset of Coronal Mass Ejections Due to Loss of Confinement  
649 of Coronal Flux Ropes. *The Astrophysical Journal* **668**, 1232–1245 (2007).
- 650 [23] Aulanier, G., Török, T., Démoulin, P. & DeLuca, E. E. FORMATION OF TORUS-  
651 UNSTABLE FLUX ROPES AND ELECTRIC CURRENTS IN ERUPTING SIG-  
652 MOIDS. *The Astrophysical Journal* **708**, 314–333 (2010).
- 653 [24] Forbes, T. G. & Isenberg, P. A. A catastrophe mechanism for coronal mass ejections.  
654 *The Astrophysical Journal* **373**, 294 (1991).
- 655 [25] Lin, J. & Forbes, T. G. Effects of reconnection on the coronal mass ejection process.  
656 *Journal of Geophysical Research: Space Physics* **105**, 2375–2392 (2000).

- 657 [26] Kliem, B., Lin, J., Forbes, T. G., Priest, E. R. & Török, T. CATASTROPHE  
658 VERSUS INSTABILITY FOR THE ERUPTION OF A TOROIDAL SOLAR MAG-  
659 NETIC FLUX ROPE. *The Astrophysical Journal* **789**, 46 (2014).
- 660 [27] Hood, A. W. & Priest, E. R. Kink instability of solar coronal loops as the cause of  
661 solar flares. *Solar Physics* **64**, 303–321 (1979).
- 662 [28] Mikic, Z., Schnack, D. D. & van Hoven, G. Dynamical evolution of twisted magnetic  
663 flux tubes. I - Equilibrium and linear stability. *The Astrophysical Journal* **361**, 690  
664 (1990).
- 665 [29] Galsgaard, K. & Nordlund, Å. Heating and activity of the solar corona: 2. Kink  
666 instability in a flux tube. *Journal of Geophysical Research: Space Physics* **102**,  
667 219–230 (1997).
- 668 [30] Aulanier, G., Démoulin, P. & Grappin, R. Equilibrium and observational properties  
669 of line-tied twisted flux tubes. *Astronomy & Astrophysics* **430**, 1067–1087 (2005).
- 670 [31] Amari, T., Luciani, J. F., Aly, J. J. & Tagger, M. Very Fast Opening of a Three-  
671 dimensional Twisted Magnetic Flux Tube. *The Astrophysical Journal* **466**, L39–L42  
672 (1996).
- 673 [32] Török, T. & Kliem, B. The evolution of twisting coronal magnetic flux tubes. *As-  
674 tronomy & Astrophysics* **406**, 1043–1059 (2003).
- 675 [33] Török, T. *et al.* Initiation of Coronal Mass Ejections by Sunspot Rotation. *Solar  
676 Physics* **286**, 453–477 (2013).
- 677 [34] Jiang, C., Feng, X., Guo, Y. & Hu, Q. Data-driven modeling of solar coronal magnetic  
678 field evolution and eruptions. *The Innovation* **3**, 100236 (2022).
- 679 [35] Moore, R. L., Sterling, A. C., Hudson, H. S. & Lemen, J. R. Onset of the Magnetic  
680 Explosion in Solar Flares and Coronal Mass Ejections. *The Astrophysical Journal*  
681 **552**, 833–848 (2001).
- 682 [36] Jiang, C. *et al.* A fundamental mechanism of solar eruption initiation. *Nature  
683 Astronomy* **5**, 1126–1138 (2021).
- 684 [37] Vršnak, B. Processes and mechanisms governing the initiation and propagation of  
685 CMEs. *Annales Geophysicae* **26**, 3089–3101 (2008).

- 686 [38] Green, L. M., Török, T., Vršnak, B., Manchester, W. & Veronig, A. The Origin,  
687 Early Evolution and Predictability of Solar Eruptions. *Space Science Reviews* **214**,  
688 46 (2018).
- 689 [39] Li, T. & Zhang, J. QUASI-PERIODIC SLIPPING MAGNETIC RECONNECTION  
690 DURING AN X-CLASS SOLAR FLARE OBSERVED BY THE *SOLAR DYNAM-*  
691 *ICS OBSERVATORY* AND *INTERFACE REGION IMAGING SPECTROGRAPH*.  
692 *The Astrophysical Journal* **804**, L8 (2015).
- 693 [40] Dudík, J. *et al.* SLIPPING MAGNETIC RECONNECTION, CHROMOSPHERIC  
694 EVAPORATION, IMPLOSION, AND PRECURSORS IN THE 2014 SEPTEMBER  
695 10 X1.6-CLASS SOLAR FLARE. *The Astrophysical Journal* **823**, 41 (2016).
- 696 [41] Duan, A. *et al.* Comparison of Two Coronal Magnetic Field Models to Reconstruct a  
697 Sigmoidal Solar Active Region with Coronal Loops. *The Astrophysical Journal* **842**,  
698 119 (2017).
- 699 [42] Shen, J., Ji, H. & Su, Y. The Precursor Phase of an X-class Flare: Magnetic Re-  
700 connection, Powering and Non-thermal Electrons. *Research in Astronomy and As-*  
701 *trophysics* **22**, 015019 (2022).
- 702 [43] Aly, J. J. How much energy can be stored in a three-dimensional force-free magnetic  
703 field? *The Astrophysical Journal* **375**, L61 (1991).
- 704 [44] Sturrock, P. A. Maximum energy of semi-infinite magnetic field configurations. *The*  
705 *Astrophysical Journal* **380**, 655 (1991).
- 706 [45] Démoulin, P., Priest, E. R. & Lonie, D. P. Three-dimensional magnetic reconnection  
707 without null points: 2. Application to twisted flux tubes. *Journal of Geophysical*  
708 *Research: Space Physics* **101**, 7631–7646 (1996).
- 709 [46] Titov, V. S., Hornig, G. & Démoulin, P. Theory of magnetic connectivity in the solar  
710 corona: THE THEORY OF MAGNETIC CONNECTIVITY. *Journal of Geophysical*  
711 *Research: Space Physics* **107**, SSH 3–1–SSH 3–13 (2002).
- 712 [47] Emslie, A. G. *et al.* GLOBAL ENERGETICS OF THIRTY-EIGHT LARGE SOLAR  
713 ERUPTIVE EVENTS. *The Astrophysical Journal* **759**, 71 (2012).
- 714 [48] Kilpua, E. K. J., Pomoell, J., Price, D., Sarkar, R. & Asvestari, E. Estimating the  
715 Magnetic Structure of an Erupting CME Flux Rope From AR12158 Using Data-  
716 Driven Modeling. *Frontiers in Astronomy and Space Sciences* **8**, 631582 (2021).

- 717 [49] Bhattacharjee, A., Huang, Y.-M., Yang, H. & Rogers, B. Fast reconnection in high-  
718 Lundquist-number plasmas due to the plasmoid Instability. *Physics of Plasmas* **16**,  
719 112102 (2009).
- 720 [50] Daughton, W. *et al.* Role of electron physics in the development of turbulent magnetic  
721 reconnection in collisionless plasmas. *Nature Physics* **7**, 539–542 (2011).
- 722 [51] Jiang, C. *et al.* Formation of Magnetic Flux Rope During Solar Eruption. I. Evolution  
723 of Toroidal Flux and Reconnection Flux. *Frontiers in Physics* **9**, 746576 (2021).
- 724 [52] He, W., Hu, Q., Jiang, C., Qiu, J. & Prasad, A. Quantitative characterization of  
725 magnetic flux rope properties for two solar eruption events. *arXiv e-prints* arX-  
726 iv:2201.03149 (2022). [2201.03149](https://arxiv.org/abs/2201.03149).
- 727 [53] Vršnak, B. Gradual Pre-eruptive Phase of Solar Coronal Eruptions. *Frontiers in*  
728 *Astronomy and Space Sciences* **6**, 28 (2019).
- 729 [54] Longcope, D. W. & Welsch, B. T. A Model for the Emergence of a Twisted Magnetic  
730 Flux Tube. *The Astrophysical Journal* **545**, 1089–1100 (2000).
- 731 [55] Gibson, S. E., Fan, Y., Mandrini, C., Fisher, G. & Demoulin, P. Observational  
732 Consequences of a Magnetic Flux Rope Emerging into the Corona. *The Astrophysical*  
733 *Journal* **617**, 600–613 (2004).
- 734 [56] Sturrock, Z., Hood, A. W., Archontis, V. & McNeill, C. M. Sunspot rotation: I. A  
735 consequence of flux emergence  $\star$ . *Astronomy & Astrophysics* **582**, A76 (2015).
- 736 [57] Fan, Y. THE EMERGENCE OF A TWISTED FLUX TUBE INTO THE SOLAR  
737 ATMOSPHERE: SUNSPOT ROTATIONS AND THE FORMATION OF A CORO-  
738 NAL FLUX ROPE. *The Astrophysical Journal* **697**, 1529–1542 (2009).
- 739 [58] Kazachenko, M. D. *et al.* SUNSPOT ROTATION, FLARE ENERGETICS, AND  
740 FLUX ROPE HELICITY: THE ERUPTIVE FLARE ON 2005 MAY 13. *The Astro-*  
741 *physical Journal* **704**, 1146–1158 (2009).
- 742 [59] Feng, X., Zhou, Y. & Wu, S. T. A Novel Numerical Implementation for Solar Wind  
743 Modeling by the Modified Conservation Element/Solution Element Method. *The*  
744 *Astrophysical Journal* **655**, 1110–1126 (2007).
- 745 [60] Jiang, C., Feng, X., Zhang, J. & Zhong, D. AMR Simulations of Magnetohydro-  
746 dynamic Problems by the CESE Method in Curvilinear Coordinates. *Solar Physics*  
747 **267**, 463–491 (2010).

- 748 [61] Jiang, C., Bian, X., Sun, T. & Feng, X. MHD Modeling of Solar Coronal Magnetic  
749 Evolution Driven by Photospheric Flow. *Frontiers in Physics* **9**, 646750 (2021).
- 750 [62] Jiang, C. & Feng, X. Preprocessing the Photospheric Vector Magnetograms for an  
751 NLFFF Extrapolation Using a Potential-Field Model and an Optimization Method.  
752 *Solar Physics* **289**, 63–77 (2014).
- 753 [63] Wiegmann, T., Inhester, B. & Sakurai, T. Preprocessing of Vector Magnetograph  
754 Data for a Nonlinear Force-Free Magnetic Field Reconstruction. *Solar Physics* **233**,  
755 215–232 (2006).
- 756 [64] Yamamoto, T. T. & Kusano, K. PREPROCESSING MAGNETIC FIELDS WITH  
757 CHROMOSPHERIC LONGITUDINAL FIELDS. *The Astrophysical Journal* **752**,  
758 126 (2012).
- 759 [65] Jiang, C. & Toriumi, S. Testing a Data-driven Active Region Evolution Model  
760 with Boundary Data at Different Heights from a Solar Magnetic Flux Emergence  
761 Simulation. *The Astrophysical Journal* **903**, 11 (2020).
- 762 [66] Jiang, C., Wu, S. T., Feng, X. & Hu, Q. Data-driven magnetohydrodynamic mod-  
763 elling of a flux-emerging active region leading to solar eruption. *NATURE COMMU-  
764 NICATIONS* 11 (2016).
- 765 [67] Schuck, P. W. Tracking Vector Magnetograms with the Magnetic Induction Equation.  
766 *The Astrophysical Journal* **683**, 1134–1152 (2008).
- 767 [68] Liu, Y. & Schuck, P. W. MAGNETIC ENERGY AND HELICITY IN TWO E-  
768 Merging Active Regions in the Sun. *The Astrophysical Journal* **761**, 105  
769 (2012).
- 770 [69] Liu, C. *et al.* THREE-DIMENSIONAL MAGNETIC RESTRUCTURING IN TWO  
771 HOMOLOGOUS SOLAR FLARES IN THE SEISMICALLY ACTIVE NOAA AR  
772 11283. *The Astrophysical Journal* **795**, 128 (2014).
- 773 [70] Harvey, K. & Harvey, J. Observations of moving magnetic features near sunspots.  
774 *Solar Physics* **28**, 61–71 (1973).
- 775 [71] Brown, D. & Walker, A. A Semi-Automatic Method to Measure the Rotation of  
776 Sunspots. *Solar Physics* **296**, 48 (2021).

777 [72] Cheung, M. C. M. & DeRosa, M. L. A METHOD FOR DATA-DRIVEN SIMULA-  
778 TIONS OF EVOLVING SOLAR ACTIVE REGIONS. *The Astrophysical Journal*  
779 **757**, 147 (2012).

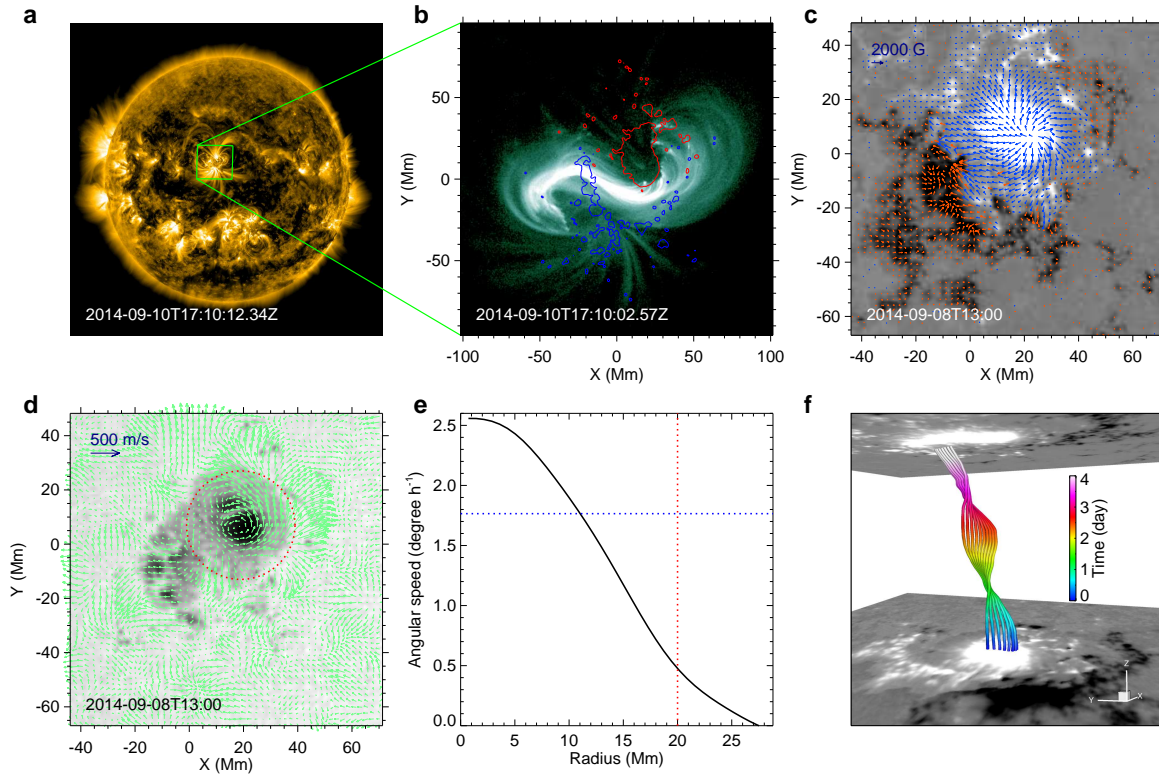


Figure 1: **Observation of coronal structure and the rotational sunspot in AR 12158.** **a**, Full-disk image of the Sun taken by SDO/AIA in 171 Å channel at 10 min before onset of the X1.6 flare. The boxed region denotes the location of the target AR. **b**, The enlarged view of the AR in SDO/AIA 94 Å channel which presents a coronal sigmoid with reverse S shape. The colored curves are shown for the contour lines of the vertical magnetic field  $B_z$ , with red (blue) representing  $B_z = 1000$  ( $-1000$ ) G. **c**, Vector magnetogram observed by SDO/HMI at two days before the flare. The arrows show the horizontal field components with blue (red) in region of  $B_z > 0$  ( $< 0$ ). **d**, Surface velocity field (the vectors colored in green) overlaid on the SDO/HMI continuum image of the AR. The main sunspot is denoted by the circle with a radius of 20 Mm. **e**, Profile of the angular speed at different radial distance from the rotation center. Here the angular speed is averaged for three days of 8–10 September 2014. The red line denotes the edge of the sunspot at 20 Mm, and the blue line denotes the angular speed of  $1.75^\circ \text{ h}^{-1}$ , which is averaged value within the radial distance of 0 to 20 Mm and thus approximates the rotation rate of the sunspot as a whole. **f**, 3D shape of the trajectories of the surface flow with the  $z$  axis representing time direction, and the color also denotes time. The bottom and top surfaces represent the magnetogram observed at 00:00 UT on 7 and 00:00 UT on 11 of September 2014, respectively.

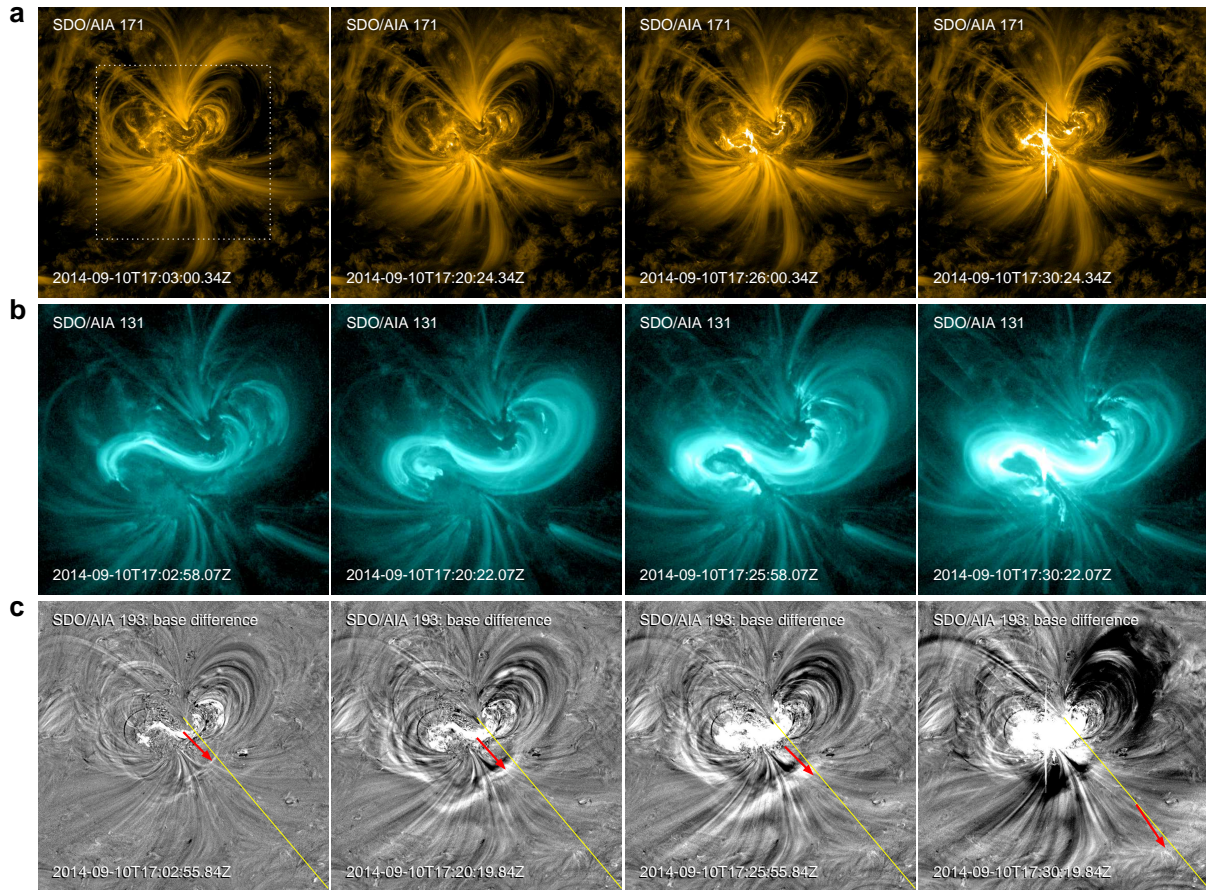


Figure 2: EUV images of the X1.6 flare taken by SDO/AIA. **a**, Images in 171 Å channel. **b**, 131 Å channel, with a smaller field of view (as denoted by the dashed box in **a**) to show the core region of the flare site. **c**, Base difference images of the 193 Å channel. The yellow line denotes the slit for which the time-distance map in Figure 3b is shown. The red arrows show the moving of an erupting loop-like structure that experienced first a slow rise well before (for around 20 min) the flare onset time and then an impulsive acceleration in the first few minutes during the flare, with more details shown in Figure 3.

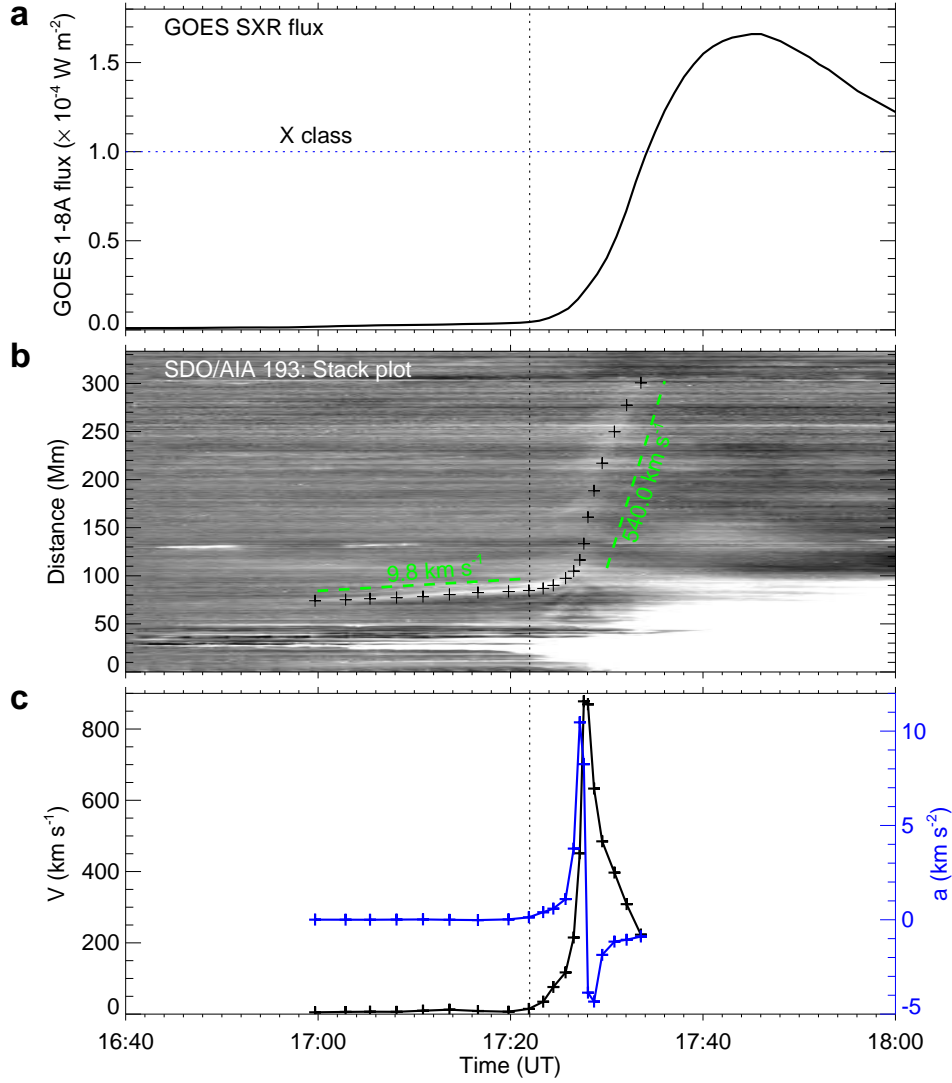


Figure 3: **Slow rise and impulsive acceleration of the erupting coronal loops.** **a**, GOES soft X-ray flux observed in the time period around the X1.6 flare. The vertical dashed line denotes the start of the fast rise of the flux. The horizontal dashed line denotes the level of flux that is defined for flare reaching X class. **b**, Time-distance stack plot for the slit as shown in Figure 2c. The plus signs overlaid are sampled to get the data of time and distance of the erupting loop-like structure, which shows first a slow rise and then an impulsive acceleration. The average speeds of the slow rise phase and the eruption phase are denoted by the green dashed lines. **c**, Evaluation of velocity and acceleration of the erupting structure as shown in **b** based on the sampled data points.

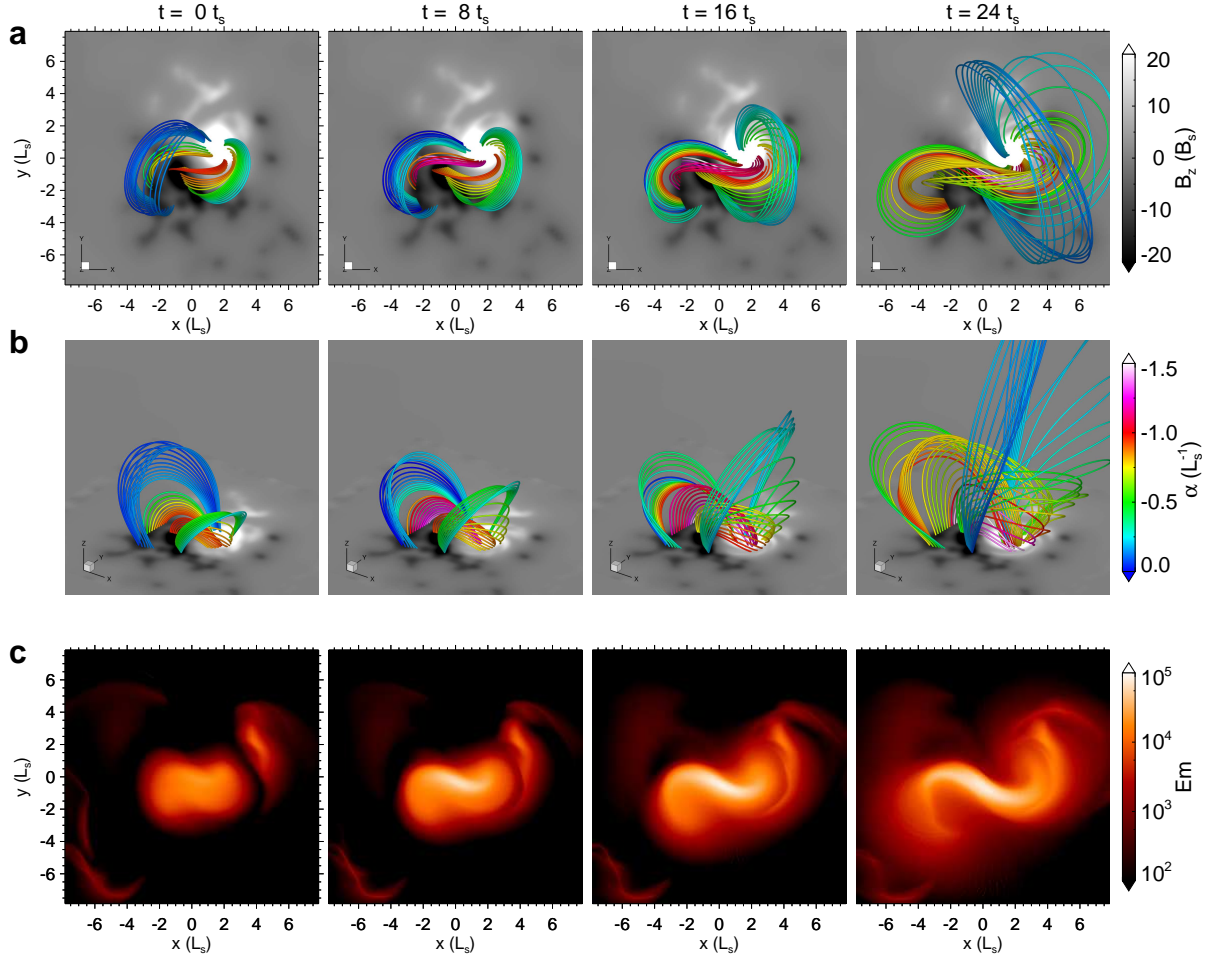


Figure 4: **Pre-eruption evolution of magnetic field and current density in the simulation with rigid rotation of the sunspot.** **a**, Top view of sampled magnetic field lines. The coloured thick curves represent magnetic field lines, and the colours denote the value of the nonlinear force-free factor defined as  $\alpha = \mathbf{J} \cdot \mathbf{B} / B^2$  where  $\mathbf{J}$  is the current density and  $\mathbf{B}$  is the magnetic field. The background shows the magnetic flux distribution on the bottom surface. Note that at different times, the field lines are traced from the same set of footpoints from the negative polarities, since they are fixed without surface motion during the simulation with the rigid rotation.  $L_s = 11.52$  Mm is the length unit,  $t_s = 105$  s the time unit, and  $B_s = 1.86$  G the magnetic field strength unit. **b**, 3D prospective view of the same field lines shown in **a**. **c**, Synthetic images of coronal emission from current density.

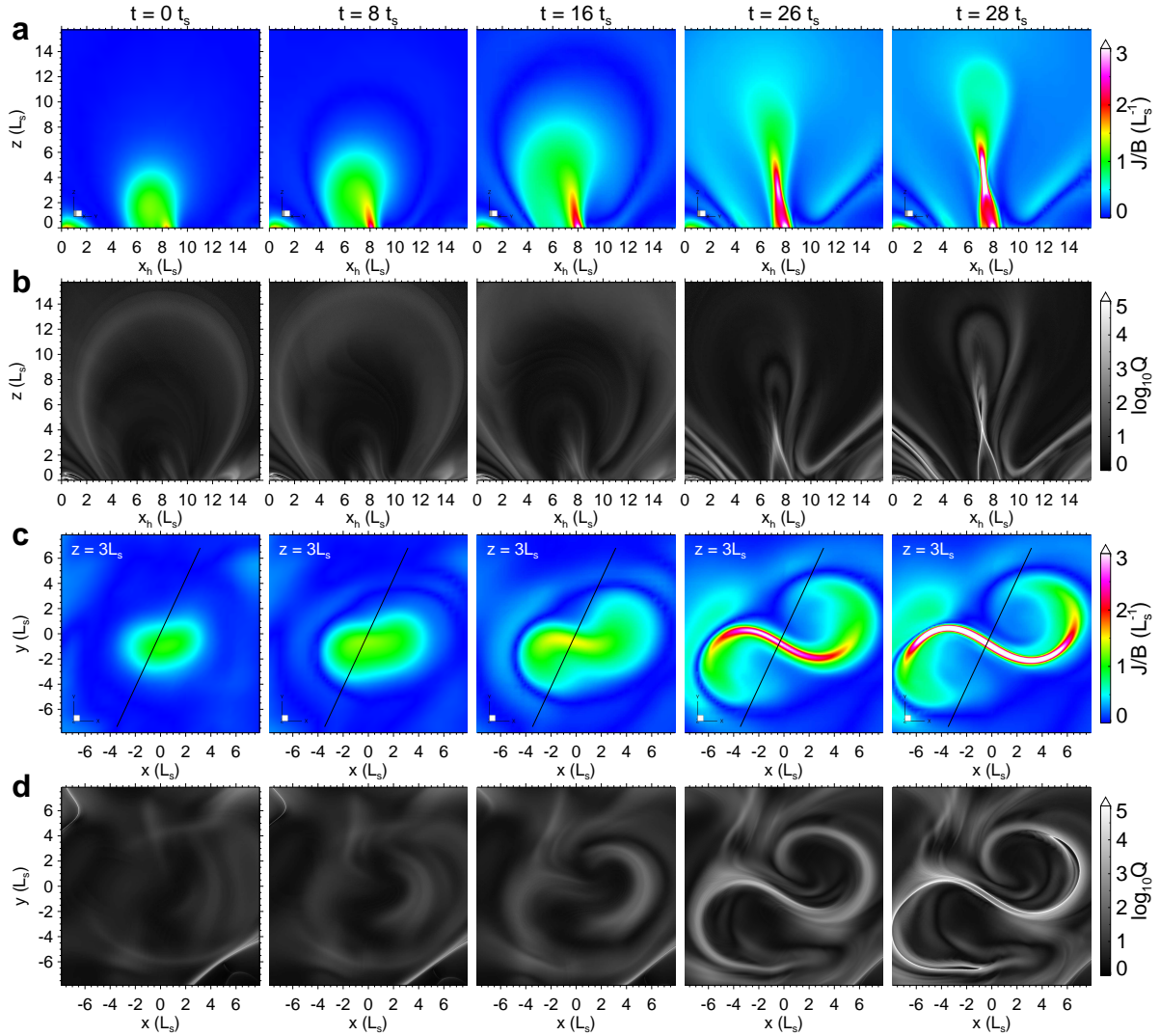


Figure 5: **Formation of the current sheet in the pre-eruption evolution phase of sunspot rigid-rotation simulation.** **a**, Vertical cross-section of the normalized current density, namely,  $J/B$ . **b**, Distribution of magnetic squashing degree (i.e.,  $Q$  factor) on the same slice of **a**. **c**, Horizontal cross-section of the normalized current density at a fixed height of  $z = 3L_s$ . **d**, Distribution of  $Q$  factor on the same slice of **d**. The projected location of the vertical cross-section in **a** and **b** is denoted by the black line in **c**.

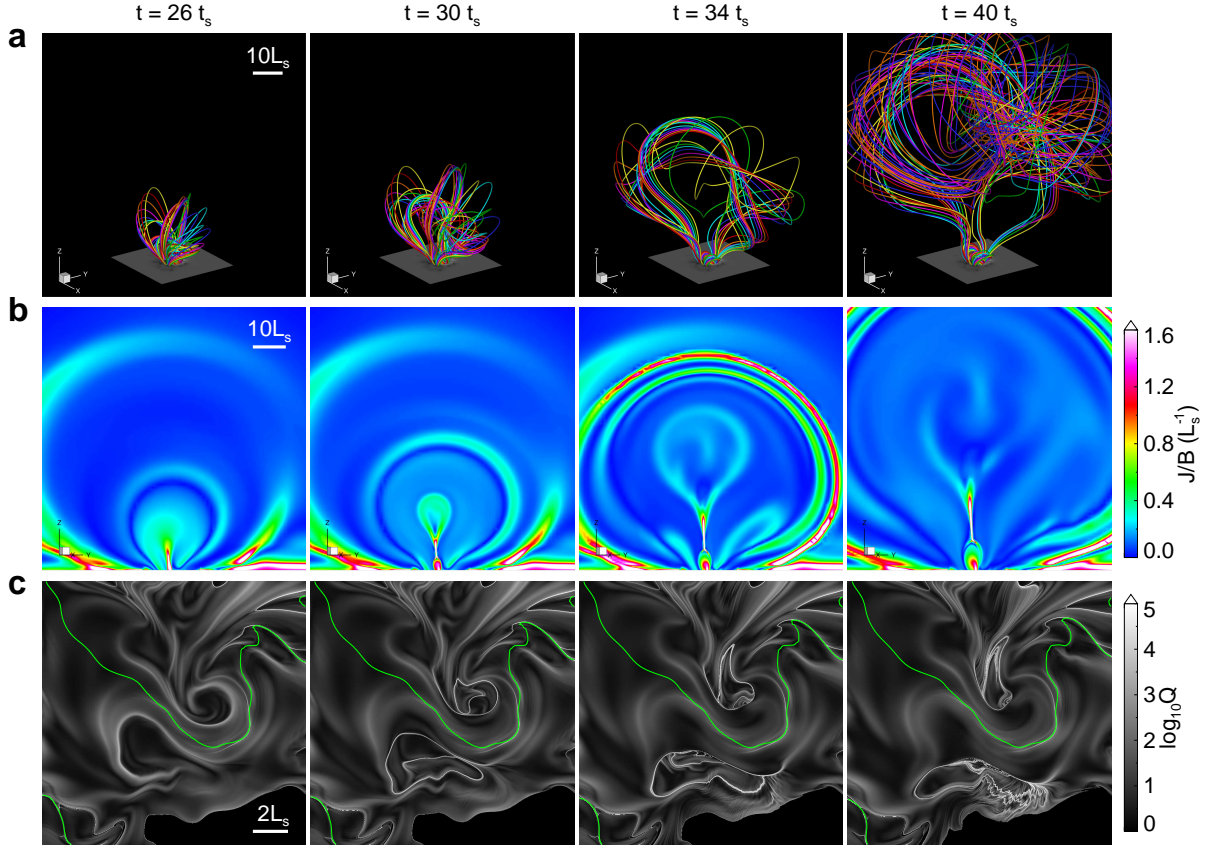


Figure 6: **Evolution of the erupting field in the sunspot rigid-rotation simulation.** **a**, Magnetic field lines are shown by the thick coloured lines, and the colours are used for a better visualization of the different lines. The bottom surface is shown with the distribution of magnetic flux. The field lines at different times are traced from the same set of footpoints from the negative polarities, since they are fixed without surface motion during the simulation with rigid rotation. **b**, Vertical central cross-section of the normalized current density. **c**, Magnetic squashing factor at the bottom surface. The green curves represent the magnetic polarity inversion line.

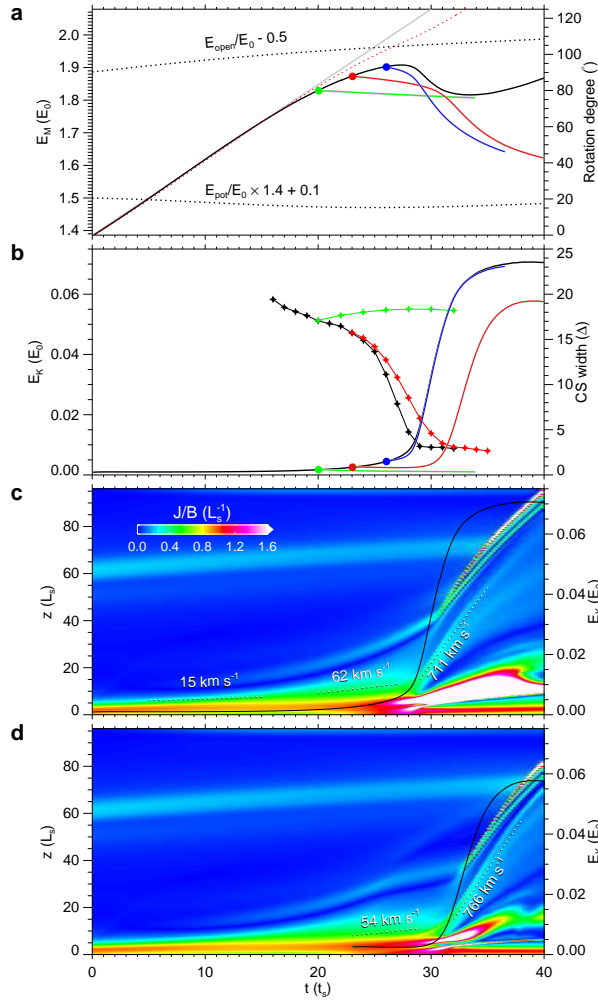


Figure 7: **Temporal evolution of different parameters in the simulation with rigid rotation of sunspot.** **a**, Magnetic energies are shown with the left  $y$ -axis. The black line shows result with continuous rotation. The gray line shows the energy injected into the volume from the bottom boundary through the surface rotational flow, that is, a time integration of total Poynting flux at the bottom surface. The green, red, and blue lines show results of runs with the rotation switched off at  $t = 20 t_s$ ,  $23 t_s$ , and  $26 t_s$ , respectively. All the energies are normalized by the initial potential field energy  $E_0$ , which is  $3.04 \times 10^{30}$  erg in the simulation, and is  $1.22 \times 10^{33}$  erg if scaled to the realistic value. The two black dashed lines show evolution of the energies of the open field (the upper one) and the potential field (the lower one). The red dashed line shows the rotational degree with the right  $y$ -axis. **b**, Kinetic energies (solid lines) with the left  $y$ -axis, and thickness of the current layer (solid lines with stars) with the right  $y$ -axis. Same as in **a**, the line colored in black, green, red, and blue show results of the continuous rotation run, and runs with the sunspot rotation stopped at  $t = 20 t_s$ ,  $23 t_s$ , and  $26 t_s$ , respectively. **c**, A time stack map of the current distribution around  $x, y = 0$  for the continuous rotation run, which is used to show the evolution speed of the erupting structure. **d**, The same time stack map of current distribution as **c** but for the simulation run with sunspot rotation stopped at  $t = 23 t_s$ . The typical speed of the structures are denoted by the dashed lines.

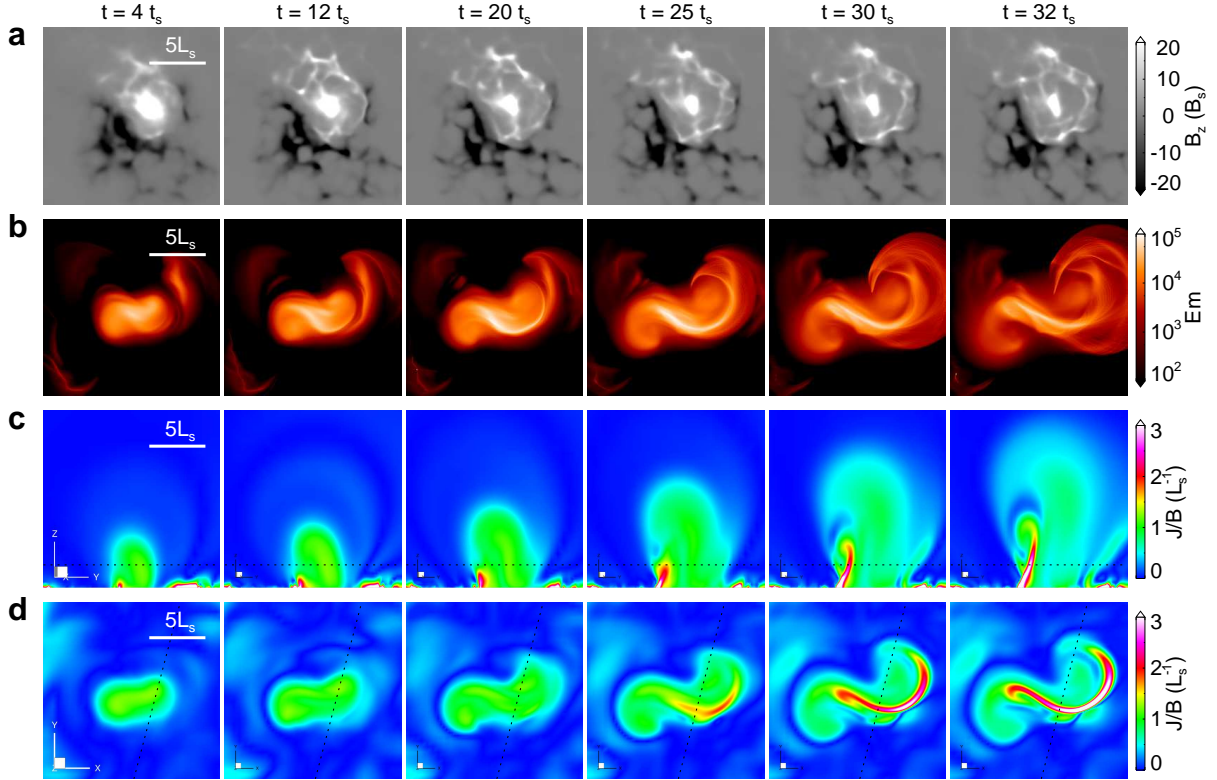


Figure 8: **Pre-eruption evolution of magnetic field and current density in the data-driven simulation.** **a**, The magnetic flux distribution at the bottom surface. **b**, Synthetic images of coronal emission from current density. **c**, Vertical cross-section of the normalized current density. **d**, Horizontal cross-section of the normalized current density. The projected location of the vertical cross-section in **c** is denoted by the black line in **d**. The height of the horizontal cross-section in **d** is shown by the black line in **c**.

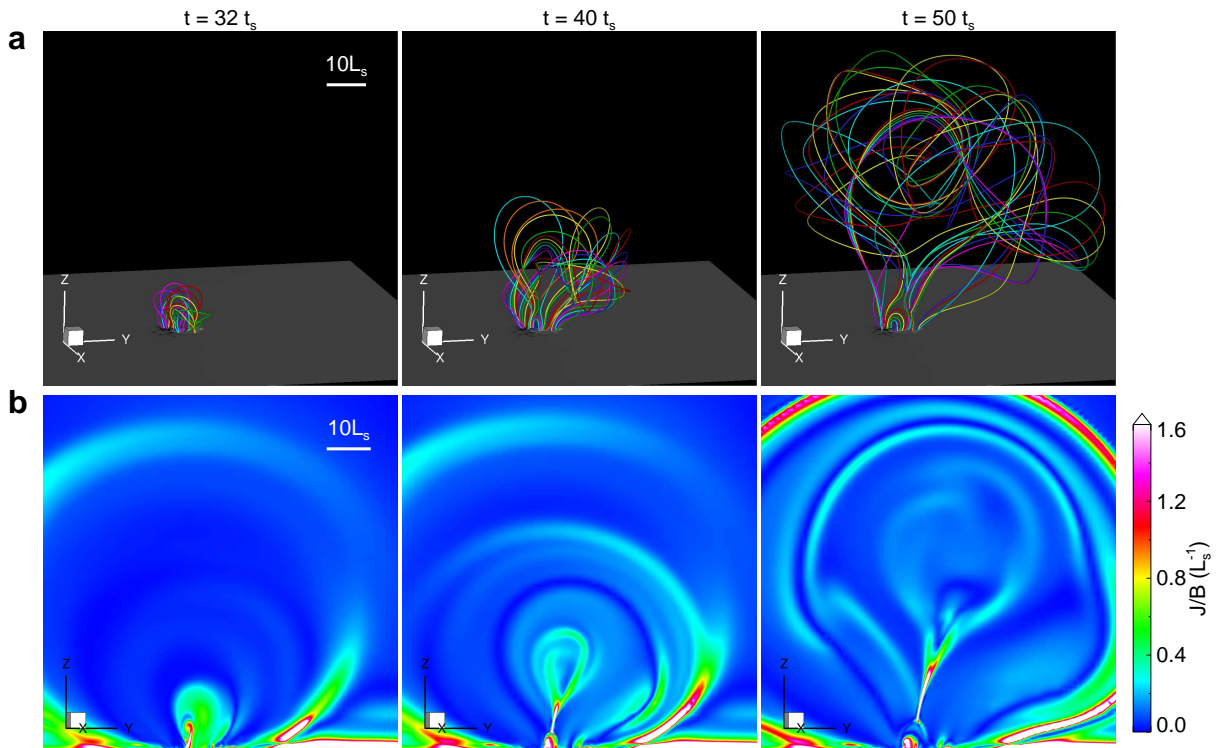


Figure 9: **Eruption in the data-driven simulation.** **a**, Evolution of magnetic field lines, which are shown by the thick coloured lines, and the colours are used for a better visualization of the different lines. **b**, Vertical cross-section of the normalized current density.

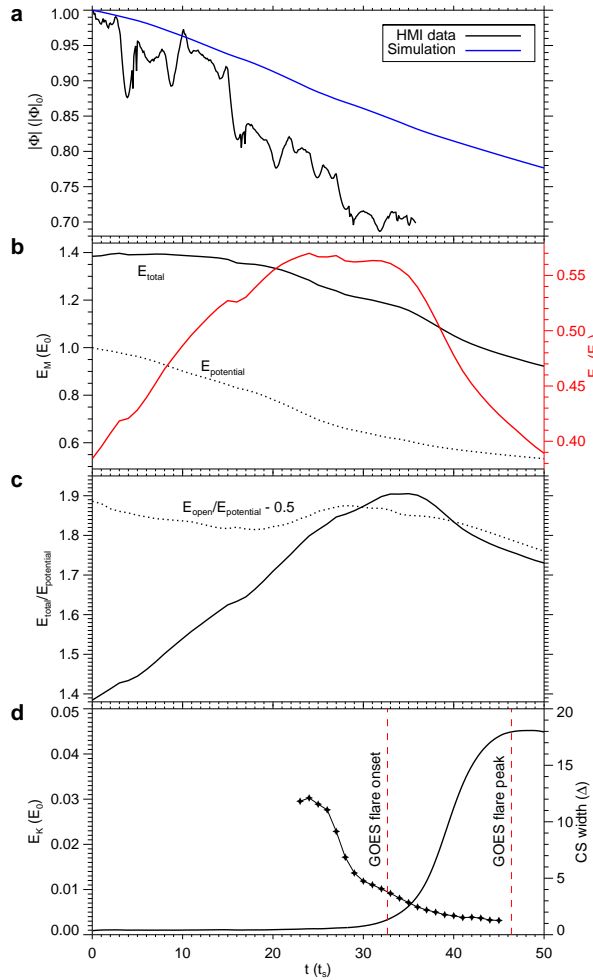
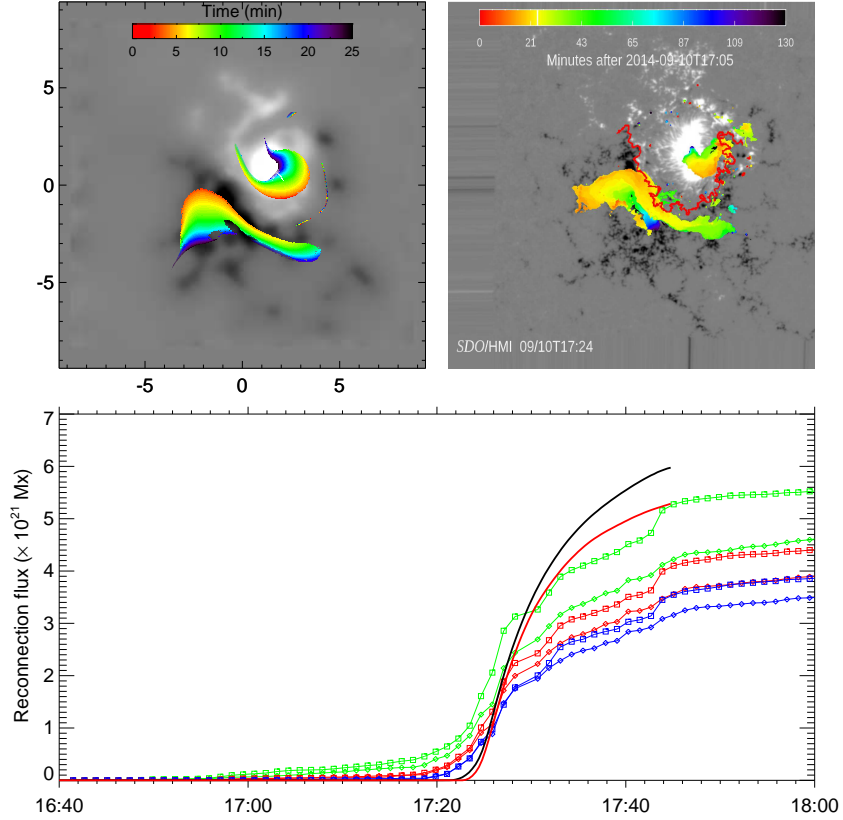
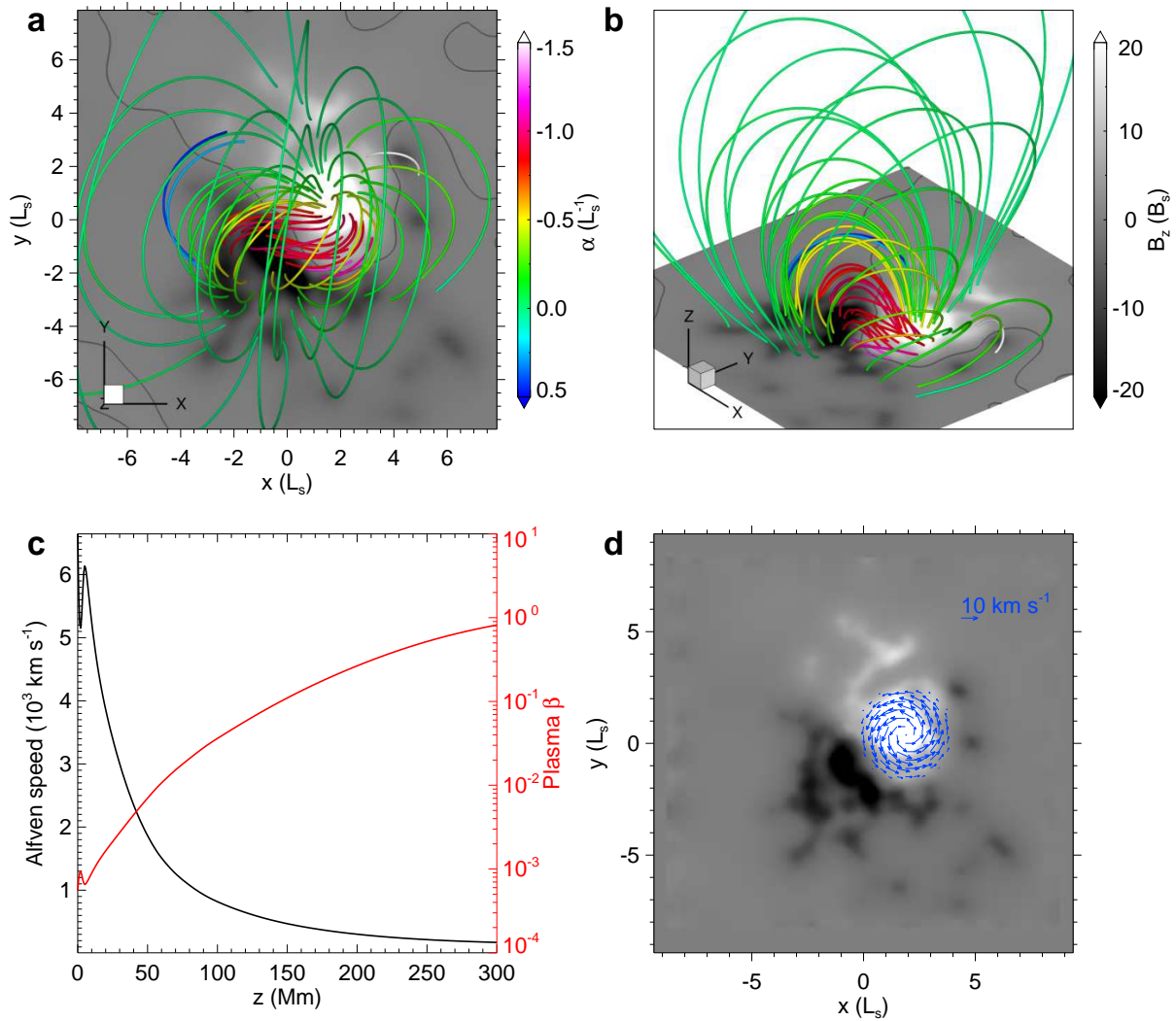


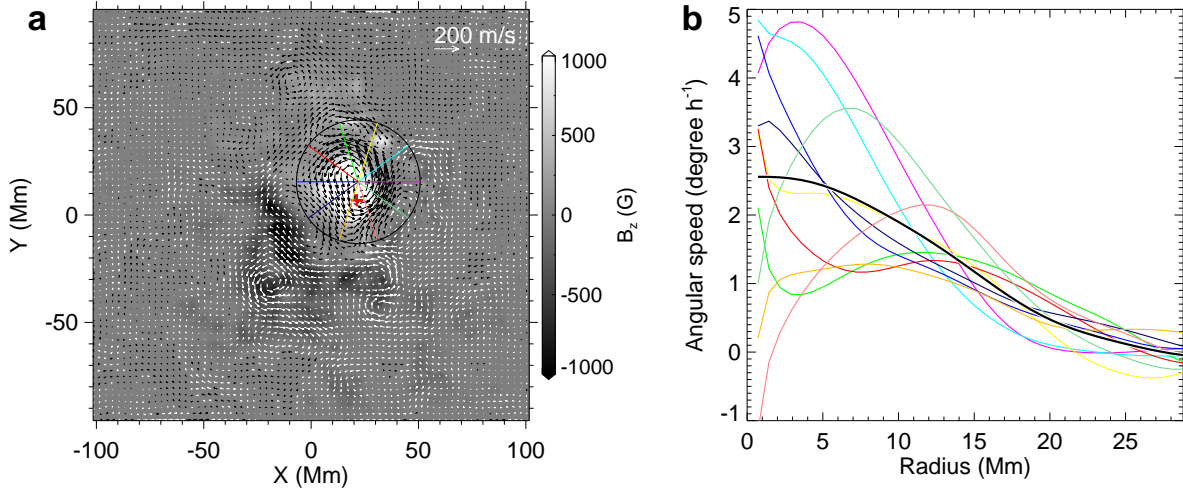
Figure 10: **Temporal evolution of different parameters in the data-driven simulation.** **a**, Total unsigned magnetic flux at the bottom surface in both observation (the black curve) and the simulation (the blue curve). Both values are normalized by their initial value at  $t = 0$ . **b**, The total magnetic energy is shown by the solid black line, and the potential field energy by the dashed black line, with  $y$ -axis on the left, and the free energy (i.e., the total magnetic energy subtracted by the potential field energy) is shown by the solid red line with the right  $y$ -axis. All the energies are normalized by the initial potential field energy at  $t = 0$ . **c**, The degree of non-potentiality of the coronal field, as measured by the ratio of total magnetic energy  $E_{\text{total}}$  to the corresponding potential field energy  $E_{\text{potential}}$ . For reference, the ratio of the open field energy to the potential field energy is shown by the dashed line. **d**, Kinetic energies with axis in the left, and width of the current layer with axis in the right. The two vertical dashed lines denote the flare onset time and peak time as recorded by GOES and scaled to the simulation time.



**Supplementary Figure 1. Comparison of reconnection fluxes derived from simulation and observation.** **a**, Temporal and spatial distribution of simulated “flare ribbons”, which are the footpoint locations of the newly reconnected field lines that forms the closed short arcades corresponding to the post-flare loops. The color denotes the time of minutes after the simulation eruption onset time. The background gray image shows the magnetic flux distribution at the bottom surface. **b**, Format same as **a** but for the observed flare ribbons as imaged in SDO/AIA 1600 Å wavelength. **c**, Evolution of reconnection flux, which is the sum of the magnetic flux in the area swept by the flare ribbons. The fluxes are counted for the positive (the thick black line) and the negative (the thick red line) polarities separately. For the observed data, three sets of results are obtained by different background removal criteria for selection of the flare ribbons, which are pixels with the intensity larger than 4 (the boxed green line), 5 (the boxed red line), and 6 (the boxed blue line) times of the background average brightness.



**Supplementary Figure 2. The initial state of the simulations.** **a**, Magnetic field lines as seen from above. The field lines are false-colored by the values of the force-free factor  $\alpha = \mathbf{J} \cdot \mathbf{B}/B^2$ . The background is shown by the magnetic flux distribution on the bottom surface, and the thick gray curves are shown for the PIL, i.e., where  $B_z = 0$ . **b**, Same as **a** but seen in a 3D perspective view. **c**, Profiles of Alfvén speed and plasma  $\beta$  with height along a vertical line with footpoint at the center of the main sunspot. **d**, The rotational flow at the bottom surface as used in the simulation with rigid rotation of the sunspot. The background is shown by the magnetic flux distribution.



**Supplementary Figure 3. Estimation of the rotation speed of the sunspot.** **a**, Vectors show the divergence-free components of the surface flow averaged for the three-day data covering 2014 September 8-10. The background image shows the magnetic flux density  $B_z$ , also averaged for the three-day HMI data. The circle denotes the rotating sunspot, and the centre of the circle is the rotating center. The radial lines are sampled to estimate the profile of angular speed of different radial distances from the circle center. Here 10 lines are shown and in the actual computation we used 100 lines with azimuthal angle distributed evenly from 0 to  $2\pi$ . The red plus symbol marks the point with the largest  $B_z$  in the sunspot. It can be regarded as the center of the sunspot and it is close to the rotation center. **b**, Profile of angular speed at different radial distance from the rotation center. The thin coloured lines denote the values along the corresponding radial lines (by the same colours) as shown in **a**. The thick line denotes the average value of all the azimuthal angles from 0 to  $2\pi$ .

## Captions for Supplementary Videos

- 781 • **Supplementary Video 1.** Evolution of total unsigned magnetic flux (top), mag-  
782 netic flux distribution (bottom left), and continuum image (bottom right) of AR  
783 12158 in four days of 7–10 September 2014.
- 784 • **Supplementary Video 2.** The flare eruption observed by SDO/AIA in different  
785 EUV wavelengths and the associated soft X-ray light curve recorded by GOES. Also  
786 an animation version for Figure 2 and Figure 3.
- 787 • **Supplementary Video 3.** Evolution of magnetic field lines (left), current densi-  
788 ty (middle), and magnetic squashing factor (right) in the simulation (for the core  
789 region) with rigid rotation of sunspot. The left two panels and correspond to the  
790 animation versions of Figure 4a and b, respectively, and the middle top panel corre-  
791 sponds to Figure 4c. The bottom middle and right panels correspond to Figure 5a  
792 and b, respectively. The top right panel corresponds to Figure 6c.
- 793 • **Supplementary Video 4.** Evolution of magnetic field lines and current density  
794 (for the whole region) in the simulation with rigid rotation of sunspot. Also an  
795 animation version for Figure 6a and b.
- 796 • **Supplementary Video 5.** Same as Supplementary Video 4 but with the sunspot  
797 rotation stopped at  $t = 23 t_s$ .
- 798 • **Supplementary Video 6.** Evolution of magnetic field lines (top), current density  
799 (bottom left), and kinetic energy (bottom right) in the data-driven simulation.

## Supplementary Files

This is a list of supplementary files associated with this preprint. Click to download.

- [SupplementaryVideo6.mp4](#)
- [SupplementaryVideo1.mp4](#)
- [SupplementaryVideo4.mp4](#)
- [SupplementaryVideo5.mp4](#)
- [SupplementaryVideo2.mp4](#)
- [SupplementaryVideo3.mp4](#)